

**Analysis of the Effects of Reduced Oxygen Atmospheres on the
Decarburization Depths of 300M Alloy Steel**

by

Steven W. Mayott

A Thesis Submitted to the Graduate
Faculty of Rensselaer Polytechnic Institute
in Partial Fulfillment of the
Requirements for the degree of
MASTER OF SCIENCE

Major Subject: MATERIALS SCIENCE AND ENGINEERING

Approved:

Dr. Roger N. Wright, Thesis Adviser

Rensselaer Polytechnic Institute
Troy, New York

July 2010
(For Graduation August 2010)

© Copyright 2010
by
Steven Mayott
All Rights Reserved

CONTENTS

LIST OF TABLES.....	v
LIST OF FIGURES.....	vi
ACKNOWLEDGMENT.....	x
ABSTRACT.....	xi
1. Introduction.....	1
1.1 Mechanisms of Decarburization.....	1
1.2 Decarburization Models without Scale.....	6
1.3 Modeling Decarburization with Scale.....	10
1.4 Stability Predictions from the Ellingham Diagram.....	11
1.5 General Assumptions.....	14
1.6 Motivation.....	15
2. Experimental Procedure.....	16
2.1 Material.....	16
2.2 Decarburizing Heat Treatment.....	16
2.2.1 Apparatus.....	16
2.2.2 Heat Treatment Procedure.....	20
2.3 Decarburization Analysis.....	23
2.3.1 Complete Decarburization Software Analysis.....	23
2.3.2 Microhardness Indentation Method.....	24
2.4 Hardening of Samples.....	26
3. Results.....	27
3.1 Decarburized Samples.....	27
3.2 Oxide Layer Analysis.....	32
3.3 Hardened Samples.....	37
4. Discussion.....	47

4.1	Comparison of Results to Estimates	47
4.2	Proposed Prediction Model	50
4.3	The Oxidation Process	57
4.4	Absence of Trends in Measured Total Decarburization Depth.....	61
4.5	Future Work	61
5.	Summary and Conclusions	63
6.	Literature Cited.....	65
7.	Appendices	67
7.1	Appendix A	67
7.2	Appendix B	68
7.3	Appendix C	73
7.4	Appendix D	75

LIST OF TABLES

Table 1.1: Estimated depths of total decarburization for three given temperatures.....	9
Table 2.1: Chemical analysis of the as-received 300M.....	17
Table 2.2: Decarburization conditions	22
Table 3.1: Ferrite depths of decarburized samples	31
Table 3.2: Scale Depth	35
Table 3.3: Total decarburization depth of the samples	45
Table 3.4: Resulting characteristic depths by sample	46
Table 4.1: Incorporation of scale on total decarburization depths	48
Table 4.2: Comparison of predicted total decarburization from Equation (20) and measured depths	56
Table 7.1: Parabolic rate constants calculated from scale depths	75

LIST OF FIGURES

Figure 1.1:	The evolution of scale formation and decarburization: a) The original condition at time = 0 upon introduction of a metal into an elevated temperature atmosphere b) The formation of a thin FeO layer and the reaction of carbon and oxygen, which forms a gas and enters the atmosphere c) The growth of the scale inward (indicated by the arrow) and the carbon monoxide diffusing through the scale to the atmosphere. The location of the original interface does not change in a) – c).	3
Figure 1.2:	The effect of scaling rate on observed decarburization depth. It can be seen that scaling rate 2, the slower of the two, results in a greater decarburization depth.	5
Figure 1.3:	Plot of estimated carbon concentrations as a function of distance from the surface at three temperatures	8
Figure 1.4:	The Ellingham diagram consisting of applicable oxide formation equations. All values are approximate. Recreated from references [6] and [14].	12
Figure 2.1:	Microstructure of the as received alloy at 1000x.	18
Figure 2.2:	Surface microstructure of the as received alloy at 100x. Note the microstructure remains uniform up to the surface.	18
Figure 2.3:	Schematic of the furnace apparatus used in the investigation	19
Figure 2.4:	Example of ferrite (complete decarburization) isolation from a micrograph.	25
Figure 2.5:	An example indentation pattern used on the decarburized samples	25
Figure 3.1:	Sample 1 (800 °C in air) surface region following heat treatment	28
Figure 3.2:	Sample 2 (900 °C in air) surface region following heat treatment, showing an increased ferrite region compared to 800 °C.	28
Figure 3.3:	Sample 3 (1000 °C in air) surface region following heat treatment. Complete decarburization increased dramatically over Sample 1.	28

Figure 3.4: Sample 4 (800 °C in 14% O ₂ , balance nitrogen) surface region. The completely decarburized region increased from Sample 1. The oxide layer is not present in this photograph.....	29
Figure 3.5: Sample 5 (900 °C in 14% O ₂ , balance nitrogen) surface region. The completely decarburized depth is very similar to Sample 2.....	29
Figure 3.6: Sample 6 (1000 °C in 14% O ₂ , balance of nitrogen) surface region. Similar to Sample 5, little change occurred from the sample in air at the same temperature.....	29
Figure 3.7: Sample 7 (800 °C in 7% O ₂ , balance nitrogen) surface region. An increase in the ferrite layer occurred in comparison to Sample 1, with a significantly reduced oxide layer.....	30
Figure 3.8: Sample 8 (900 °C in 7% O ₂ , nitrogen balance) surface region. The reduced oxygen atmosphere had little to no effect in comparison to temperature.....	30
Figure 3.9: Sample 9 (1000 °C in 7% O ₂ , nitrogen balance) surface region. The ferrite region is approximately equal to the other two samples (3 and 6) heat treated at 1000 °C.....	30
Figure 3.10: Microstructure of Sample 6 displaying oriented coarse pearlite taken at 1000x	33
Figure 3.11: Microstructure of Sample 9 taken at 1000x.....	34
Figure 3.12: The oxide layers present in Sample 1	36
Figure 3.13: Sample consisting of an oxide of unknown stoichiometry	36
Figure 3.14: Hardness profile of the hardened as-received sample	38
Figure 3.15: Representative microstructure of a hardened sample	39
Figure 3.16: Hardness profile of Sample 1	40
Figure 3.17: Hardness profile of Sample 2	40
Figure 3.18: Hardness profile of Sample 3	41
Figure 3.19: Hardness profile of Sample 4	41
Figure 3.20: Hardness profile of Sample 5	42
Figure 3.21: Hardness profile of Sample 6	42

Figure 3.22: Hardness profile of Sample 7	43
Figure 3.23: Hardness profile of Sample 8	43
Figure 3.24: Hardness profile of Sample 9	44
Figure 4.1: Natural log of total decarburization depth vs. reciprocal temperature to allow creation of an Arrhenius equation for 21% O ₂	51
Figure 4.2: Natural log of total decarburization depth vs. reciprocal temperature to allow creation of an Arrhenius equation for 14% O ₂	52
Figure 4.3: Natural log of total decarburization depth vs. reciprocal temperature to allow creation of an Arrhenius equation for 7% O ₂	53
Figure 4.4: Plot of activation energies vs. oxygen concentrations to allow creation of a best fit polynomial	54
Figure 4.5: Plot of the pre-exponential constant vs. oxygen concentration to allow creation of a best fit polynomial	54
Figure 4.6: The iron-oxygen phase diagram. Reproduced from N. Birks., G. H. Meier, and F. S. Pettit. <i>Introduction to the High-temperature Oxidation of Metals</i> . 2nd ed. New York: Cambridge University Press, 2006. Print.....	58
Figure 4.7: The two oxide layers formed on the surface of Sample 3. Taken at 200x.	59
Figure 7.1: Concentration gradient of a carbon steel created from a Fourier series	67
Figure 7.2: Hardness profile prior to austenitization and quenching of Sample 1	68
Figure 7.3: Hardness profile prior to austenitization and quenching of Sample 2	69
Figure 7.4: Hardness profile prior to austenitization and quenching of Sample 3	69
Figure 7.5: Hardness profile prior to austenitization and quenching of Sample 4	70
Figure 7.6: Hardness profile prior to austenitization and quenching of Sample 5	70
Figure 7.7: Hardness profile prior to austenitization and quenching of Sample 6	71
Figure 7.8: Hardness profile prior to austenitization and quenching of Sample 7	71
Figure 7.9: Hardness profile prior to austenitization and quenching of Sample 8	72
Figure 7.10: Hardness profile prior to austenitization and quenching of Sample 9	72
Figure 7.11: Micrograph of Sample 1 (800 °C in air, furnace cooled)	73

Figure 7.12: Micrograph of Sample 2 (900 °C in air, furnace cooled) 74

Figure 7.13 Micrograph of Sample 9 (1000 °C in 7% O₂, balance nitrogen, furnace cooled) 74

ACKNOWLEDGMENT

The author wishes to express gratitude to Dr. Roger N. Wright for allowing the research of a metallurgy based topic over the last year and a half. In a field where the newest and most advanced materials often gain the majority of funding, Dr. Wright seemed to be one of the few professors who remained loyal to the advancement of metals.

The FIERF program and Canton Drop Forge deserve many thanks for contributing funding and allowing this project to occur.

Mr. Rob Planty was always very helpful throughout the metallography process and Mr. Don VanSteele for assistance in the experimental set up. The author would like to acknowledge and thank them for their assistance.

The author also would like to thank his mother, Dale A. Mayott, for constantly providing the utmost support. She was a driving force in times of doubt to the author pursuing a Master's degree and has always been an advocate of higher education.

Last, but certainly not least, the author would like to thank his father, the late Warren E. Mayott, who served as an inspiration during difficult times throughout the past five years at RPI. A fellow of the AWS, his deep knowledge in the field of metallurgy and welding always served as a model of excellence to strive for and provided vast motivation.

ABSTRACT

The influence of temperature and atmospheric oxygen concentration on the depths of decarburization (the kinetic process in which carbon diffuses from the near surface region in carbon-containing metals) is investigated in the following study. Samples of forged 300M steel alloy were purposely decarburized for two hours at 800, 900, and 1000 °C, each in air, 14% O₂ with a balance of nitrogen, and 7% O₂ with a balance of nitrogen. The complete decarburization (ferrite) depth was estimated using a visual estimation and software estimation method. Samples were then hardened via austenitization at 1000 °C for 30 minutes in a 1.33×10^{-5} Pa vacuum and immediately quenched in water to enhance the hardness gradient, which is directly related to the carbon concentration profile. A Vickers microhardness indentation test was used to produce such hardness gradients and allowed estimation of the total decarburization depth, that is, the depth from the surface which is adversely affected by decarburization. These depths were then compared to values predicted from error functions with and without the incorporation of the oxide layer (scale). An algorithm specific to these conditions and material was produced, allowing input of time, temperature, and atmospheric oxygen content.

As predicted in the literature, atmospheric oxygen concentrations of these amounts were ultimately concluded to have no major effect on either complete or total decarburization depths and temperature had the most pronounced effect. However, the oxide layer was found to decrease in both the 14% and 7% O₂ conditions at all temperatures, which the literature predicted would not occur until very low partial pressures of oxygen. Further, this reduced scale depth did not increase decarburization, indicating the diffusion of carbon monoxide through the oxide layers was not a rate limiting step.

1. Introduction

It has long been known that the process of decarburization leads to harmful effects if not dealt with through a secondary process such as pickling or shaving. This phenomenon therefore contributes to wasted material, time, and ultimately money in an industrial setting. Decarburization, the kinetic process in which carbon diffuses from the surface of a metal (typically steel), weakens the surface layer of the specimen since the hardness, i.e. strength, of a steel is dependent mainly on the carbon content and phases present. The diffusion of carbon from steel only becomes prominent at elevated temperatures such as those present in heat treatments occurring in the austenite (γ) region and also the austenite and ferrite ($\gamma + \alpha$) region of an iron-carbon phase diagram. The deleterious effects of decarburization are not just limited to a decrease in tensile strength, but have also been reported to increase shear strain below the surface, increase the rate of crack growth, increase the wear rate, and decrease fatigue resistance.^{[1],[2]}

In a plain carbon steel, below 910 °C the carbon content will decrease at the surface until a layer of ferrite is formed and continues to form at the expense of the austenite.^[3] This ferrite layer then acts as a barrier to additional decarburization due to the low solubility of carbon in ferrite.^[4] Using such logic, it can be assumed that below the eutectoid temperature (727 °C), where austenite is no longer present, there would be a significant decrease in decarburization owing to a ferrite layer and lack of the relatively high carbon-soluble austenite phase. The austenite phase may be considered extremely prone to decarburization in most circumstances.

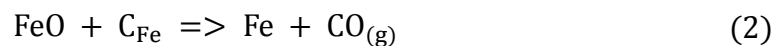
1.1 Mechanisms of Decarburization

Decarburization may be avoided if the correct atmosphere is chosen, although time and temperature are the two most important variables.^[5] It is very common for steel to be heat treated in oxidizing environments, especially in an industrial setting. Take for example the introduction of plain carbon steel into air at an elevated temperature (> 910 °C). Initially, the metal will react with the oxygen (O_2) through the reaction:



where M is a metal, iron in this case. The product, MO, is a solid and in this specific case will take the form FeO. Oxygen will also interact in a similar manner with carbon to form either carbon monoxide or carbon dioxide. This, however, is a gas and will disperse into the atmosphere once the reaction has occurred. It should be noted that iron is much more abundant than carbon in the metal. The result is a thin carbon absent iron-oxide layer. The reaction of iron or carbon and oxygen will continue at the FeO-steel interface, but with the added step of either the iron (or carbon) passing through the iron oxide layer (the “scale”), or oxygen passing through towards the steel. The increasing depth of the scale occurs at the expense of the steel, driving the interface inward. A summary of the above is depicted in Figure 1.1.

Decarburization begins to occur as the rate of carbon being consumed by the reaction with oxygen exceeds the growth of the scale. Additional carbon begins to be drawn to the scale from more interior depths. This mainly occurs because in addition to reacting with gaseous oxygen that has diffused through the scale, it begins to react with the scale at the interface. The iron-oxide layer which forms contributes to decarburization through the reaction:



where C is in solution in the steel.^[6] The oxide layer need not be FeO; it may also be Fe₃O₄ or Fe₂O₃ (in order of increasing oxidation rate). Such a reaction may only occur if the carbon monoxide can escape through the scale, as it is originally formed at the scale-steel interface and travels through the scale to the atmosphere. Thus, the permeability of the scale can have a large effect on decarburization. In fact, a scale of greatly reduced permeability has been formed through careful heating and prevented diffusion of carbon monoxide.^[7] This resulted in carbon enrichment at the surface rather than decarburization. However, in general the scale is quite porous and the removal of the carbon monoxide is achieved.

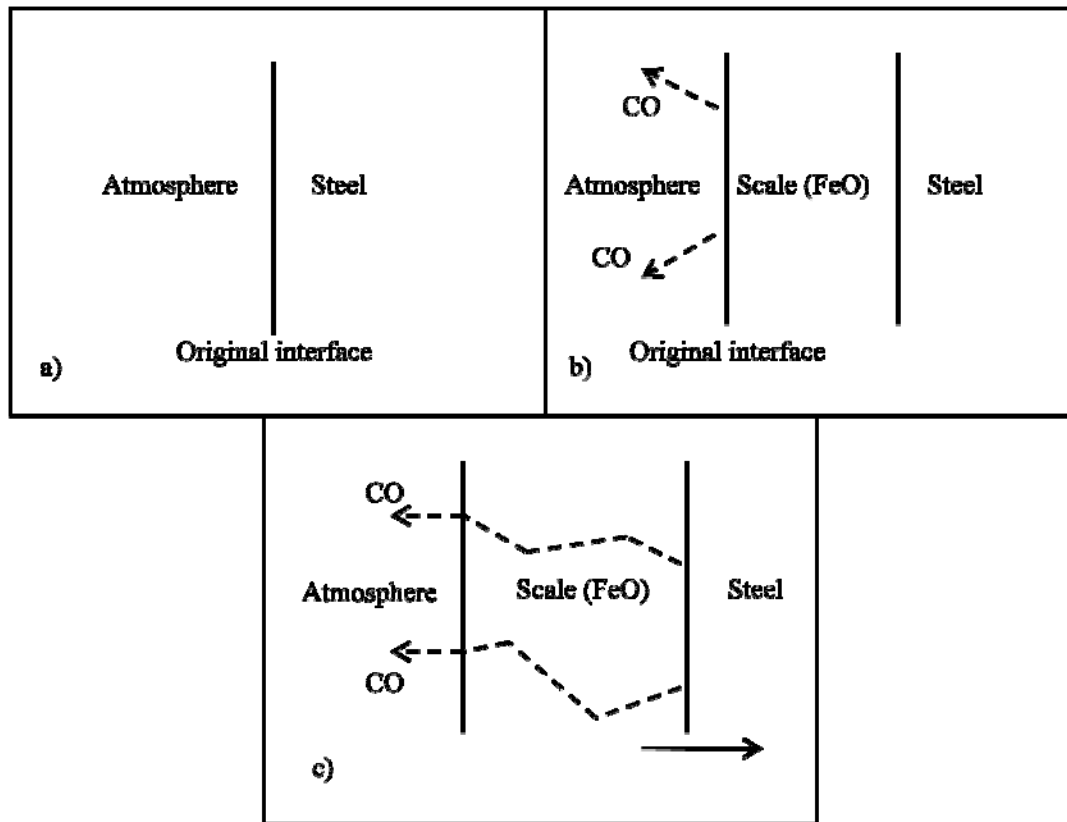


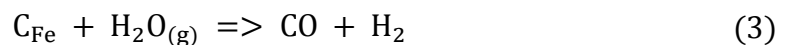
Figure 1.1: The evolution of scale formation and decarburization: a) The original condition at time = 0 upon introduction of a metal into an elevated temperature atmosphere b) The formation of a thin FeO layer and the reaction of carbon and oxygen, which forms a gas and enters the atmosphere c) The growth of the scale inward (indicated by the arrow) and the carbon monoxide diffusing through the scale to the atmosphere. The location of the original interface does not change in a) – c).

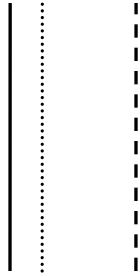
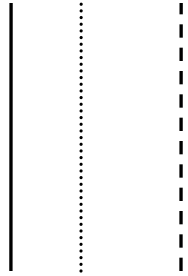
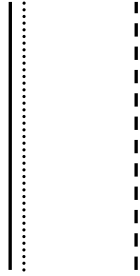
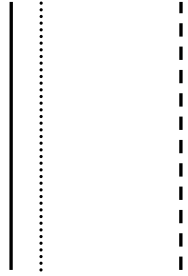
Because the carbon monoxide must diffuse through the scale, one might assume that as this layer increases the decarburization rate may decrease due to the increased path length required. Even in the presence of a high oxygen atmosphere where the source is plentiful, the arrival of oxygen may be limited. However, if decreasing the atmospheric oxygen concentration slows the rate of scale growth, decarburization may actually increase despite less oxygen being available. This may be explained by picturing carbon being drawn to the scale-metal interface at the same rate as the previous scaling rate, but the remaining pure iron at the interface not being transformed to FeO as quickly. The result is an increased decarburization depth. Figure 1.2 serves to clarify this principle. In addition, the following is a very suitable explanation:

One of the most common fallacies is to attempt to reduce decarburization by reducing the oxygen potential in the furnace. Since the carbon content at the metal-scale interface is constant, so long as FeO remains in contact with the steel, the driving force for carbon diffusion is also constant in the presence of a scale. However, by reducing the oxygen potential of the atmosphere, the scaling rate can be reduced and this will affect the observed depth of decarburization. (Birks, Meier, and Pettit 156)

It has in fact been observed that more severe decarburization frequently occurs in non-scaling atmospheres than that in scaling conditions.^[8] Carbon *dioxide* may also form from carbon monoxide by interaction with the scale or from additional interaction with oxygen in the atmosphere.^[9]

However, decarburization is not simply dependent on the presence of oxygen. Interactions of the steel with H₂O and CO₂ may occur through the reactions:^[10]



Scaling rate 1			
Scaling rate 2			
	Time = 0	Time 1	Time 2

 = original atmosphere-metal interface
  = scale-metal interface
  = decarburization front

Figure 1.2: The effect of scaling rate on observed decarburization depth. It can be seen that scaling rate 2, the slower of the two, results in a greater decarburization depth.

- Notes:
- 1) Decarburization depth is equal to the distance from the scale-metal interface to the decarburization front
 - 2) Scaling rate 1 > scaling rate 2
 - 3) Time = 0 < Time 1 < Time 2

Because carbon monoxide is more stable than carbon dioxide when exposed to high temperatures, an environment in which the ratio of partial pressures of CO:CO₂ is maximized will minimize decarburization in the absence of a scale. This is because the carbon monoxide will not noticeably react with the steel. However, the carbon dioxide will presumably react with the carbon in the steel to form CO. The minimum ratio to eliminate decarburization in such environments at 1050 °C is derived to be approximately 140 in the paper *Mechanisms of Decarburization* by Neil Birks (1970).^[4] However, in an oxidizing environment Equation (2) will be the primary mechanism of carbon removal when a scale is present. Thus oxidizing environments were the focus of this investigation.

1.2 Decarburization Models without Scale

Fick's second law typically serves as an adequate basis of diffusion modeling in decarburization studies:

$$\frac{\partial C}{\partial t} = D \frac{\partial^2 C}{\partial x^2} \quad (5)$$

where C represents the concentration of an element at time t , D is the diffusion coefficient of that element in a material, and x is the position of interest. The diffusion coefficient is typically dependent on many factors such as material structure, alloying elements, but mainly temperature, and may be expressed as:

$$D = D_0 \exp\left(-\frac{Q_D}{RT}\right) \quad (6)$$

where D_0 is a temperature independent pre-exponential factor (m²/s), Q_D is the activation energy for diffusion (J/mol), R is the gas constant of 8.314 (J/mol), and T is the temperature (K). For carbon diffusing in FCC iron (austenite), the diffusion coefficient may be expressed as:^[11]

$$D = 2.3 \times 10^{-5} \exp\left(-\frac{148,000}{8.314T}\right) \quad (7)$$

It is then necessary to apply the boundary conditions to Equation (5):

$$C = C_0 \text{ for } x > 0; t = 0 \quad (8)$$

$$C = C_s \text{ for } x = 0; t > 0 \quad (9)$$

where C_0 is the concentration of carbon at $t = 0$, equal to that carbon concentration of the bulk anywhere in the sample, and C_s is the carbon concentration at the surface, equal to 0 in most basic cases of decarburization. Solving Fick's second law for the concentration at any point and time yields the relationship:^[12]

$$\frac{C}{C_0} = \operatorname{erf}\left(\frac{x}{2\sqrt{Dt}}\right) \quad (10)$$

This form assumes that the surface concentration, typically denoted as C_s , is equal to 0. It should be observed that this formula indicates the concentration at position x is completely dependent on time and temperature (via the diffusion coefficient).

In this investigation, steel samples of 0.39 wt% carbon were initially decarburized for $t = 7200$ s (2 hours) at temperatures of 800, 900, and 1000 °C in air for baseline comparisons. The predicted carbon concentration profiles are depicted graphically in Figure 1.3 for a similar composition steel (0.4% carbon) under these conditions.

In addition, the depth of total decarburization may be estimated through isolating x in Equation (10). The total depth of decarburization is rarely selected to correlate to 100% of the original carbon value, but rather a lesser, arbitrary percentage. In this investigation, this value was chosen to be 90%. Therefore, C / C_0 is set to 0.9. Inserting the correct diffusion coefficient, D , and time, t , will then allow calculation of the depth at which 90% carbon is achieved. These values are displayed in Table 1.1.

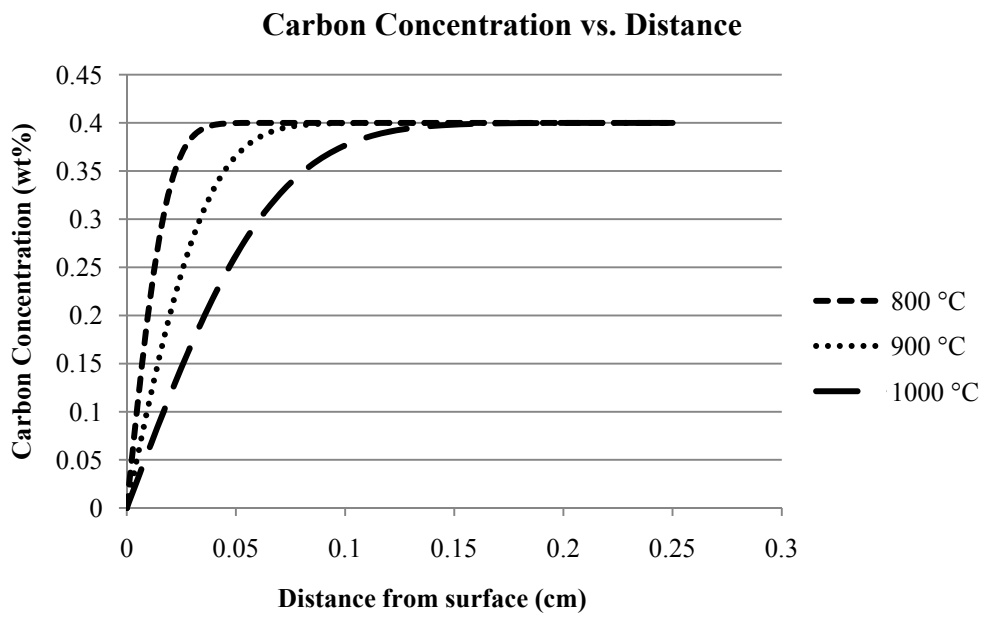


Figure 1.3: Plot of estimated carbon concentrations as a function of distance from the surface at three temperatures

Table 1.1: Estimated depths of total decarburization for three given temperatures

Temperature (°C)	Diffusion Coefficient (10^{-12} m ² /s)	Estimated Depth of Decarburization (mm)
800	1.43	0.23
900	5.90	0.48
1000	19.40	0.87

Fick's second law may also be solved via a Fourier series (Appendix A). However, simple predictions as shown in Table 1 are not as easily computed. Because of its ease of use and simplicity, the error function in Equation (10) remains the standard decarburization model.

1.3 Modeling Decarburization with Scale

Although Equation (10) is a fairly accurate model in decarburization studies, it does not take into consideration the scale formed during exposure to elevated temperatures. Such a layer acts as a simultaneous source to the formation of carbon monoxide and a barrier to the removal of it. Equation (10) only represents the diffusion of carbon through FCC iron by "random jumps," and not the additional barrier of the scale. Such random jumps are dependent on the thermal energy, interstitial sites available, and activation energy of a carbon atom leaving its initial site.

The effect of adding a scaling factor into a decarburization model was proposed by N. Birk:^[4]

$$\frac{C_0 - C}{C_0 - C_S} = \frac{\operatorname{erfc}\left(\frac{x}{2\sqrt{D_C t}}\right)}{\operatorname{erfc}\left(\frac{k_c}{2D_C}\right)^{\frac{1}{2}}} \quad (11)$$

where k_c is the parabolic rate constant, which is a function of the depth of metal consumed by scale formation, X , in time t :

$$k_c = \frac{X^2}{2t} \quad (12)$$

Equation (11) predicts a concentration gradient of metal affected by both scale formation and decarburization. The rate constant given in Equation (12), in theory, will be relatively unaffected by the external oxygen partial pressure.^[6] It has been suggested

that in order to observe a significant difference in the rate constant in the FeO scale above 570 °C, an oxygen partial pressure of approximately 10^{-12} atm at 1000 °C is required. The only layer that would be affected by this is the most exterior, haematite (Fe_2O_3) layer, accounting for only approximately 1% of the metal-scale thickness. This is obviously a large reduction in oxygen presence to begin observing significant effects and implies that reducing the concentration to even 1% (in comparison to air, consisting of 21%) should have little effect on the scale rate, and therefore the decarburization for a constant time and temperature. Further, the rate constant is dependent on temperature following an Arrhenius relationship:^[13]

$$k_c = k_0 \exp\left(-\frac{Q}{RT}\right) \quad (13)$$

where Q is the activation energy, and k_0 is a temperature independent pre-exponential factor. In the end, to predict decarburization with scaling involved it is essential to know the rate of scale growth in so far as it further complicates decarburization.

Birk also went on to propose that ultimately the depth of decarburization for a eutectoid steel in air, not including the scale, in the temperature range of 900 – 1300 °C could be predicted by Equation (14):^[6]

$$d = 10.5 \exp\left(-\frac{8710}{T}\right) t^{\frac{1}{2}} \text{ mm} \quad (14)$$

Other steels could also be represented with a similar equation, but with the difference being in the pre-exponential constant.

1.4 Stability Predictions from the Ellingham Diagram

The Ellingham diagram allows immediate prediction of the stability of oxides at given temperatures. Such a diagram has been reconstructed for the applicable reactions in Figure 1.4. It is assumed the reader has some knowledge of Ellingham diagrams. The potential reactions which are believed to occur in this investigation consist of:^[14]

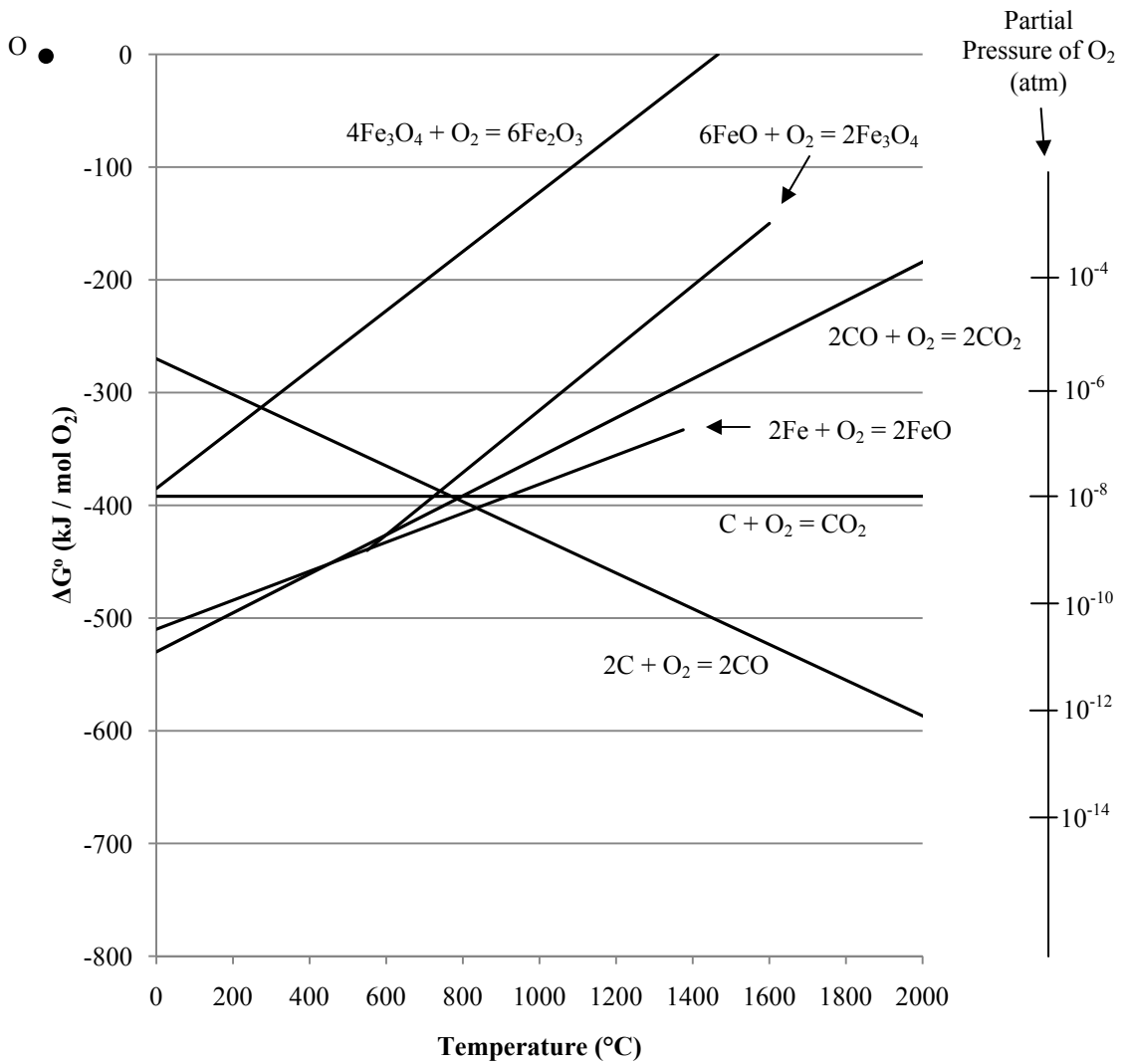
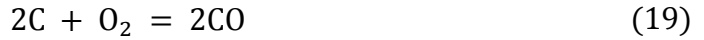


Figure 1.4: The Ellingham diagram consisting of applicable oxide formation equations. All values are approximate. Recreated from references [6] and [14].



The first step to apply this to the current study is ensuring the partial pressures of oxygen involved are above the minimal partial pressures required for oxidation to occur. Equation (15) requires the highest minimum partial pressure at 1000 °C with a value of approximately 10^{-5} atm. At 7% oxygen and a balance of nitrogen yielding the lowest partial pressure of this investigation, conditions are far above 10^{-5} atm and therefore the above reactions are possible from this perspective.

It can be observed that the Ellingham diagram suggests at room temperature to approximately 570 °C Equation (16) will be the most stable oxidation of iron, as it has the lowest Gibbs free energy. This indicates that as FeO is formed it should further combine with oxygen to form Fe_3O_4 . Therefore, FeO is a metastable phase and should not be present for extended times below 570 °C. This is further discussed and confirmed in section 4.3. Above this temperature, Equation (17) produces the most stable iron oxide. This also suggests that above 570 °C the Fe_3O_4 may combine further with an iron atom to create 4FeO , as it is the oxide closest to the steel up until this point. At all temperatures, Equation (15) is the least stable oxide reaction, and would therefore not occur until there is a lack of available iron to form the other oxides.

Carbon is within the steel and is not readily available for oxidation. Therefore, it requires an additional step to become oxidized in the form of CO_2 or CO. This step may alter the free energies on the Ellingham diagram. At temperatures below 700 °C, $2\text{CO} +$

$O_2 = 2CO_2$ (Equation (18)) is more stable. Above this temperature, $2C + O_2 = 2CO$ (Equation (19)) becomes the more stable of the two. It should be noted that this equation is the only one on the Ellingham diagram whose stability actually increases with temperature, causing a negative slope. Although $2CO + O_2 = 2CO_2$ is the most stable at lower temperatures, it requires the formation of carbon monoxide. However, carbon monoxide is not the most stable form until above 700 °C, at which temperature equation $2C + O_2 = 2CO$ is more stable than $2CO + O_2 = 2CO_2$ regardless. Thus formation of carbon dioxide from carbon monoxide and oxygen (Equation (20)) is not likely.

Because this experiment involved heating of samples through all the temperatures previously discussed, the reactions occurring constantly change and there is not one reaction which can fully describe the oxidation of iron or carbon. The mechanism of decarburization, in theory, should change approximately half way through heating.

1.5 General Assumptions

During the radiant heating of material with significant cross section, the surface is typically 20 – 50 °C hotter than the center.^[4] This additional heat supplies the surface and near surface carbon atoms with additional thermal energy, allowing them to make more successful jumps. Because of this, an increase in decarburization is expected to occur during this scenario. In the case of smaller samples being held at temperature for extended amounts of time, such as in this investigation, it may be assumed that the sample is uniformly heated.

When a sample is left in a furnace for the duration of the heating, dwelling, and cooling cycle, it is exposed to the whole range of temperatures in which the diffusion rate will drastically change and possible phase transformations will occur. In steel, such a phase transformation begins at approximately 727 °C. As discussed earlier, at temperatures below this a thin ferrite layer is initially formed and acts as a barrier to further decarburization due to the low carbon solubility of ferrite. Thus from room temperature to 727 °C very little decarburization is expected. Above this temperature, austenite will begin to form and contribute more significantly to decarburization until the target temperature is reached. As the temperature increases in this region, diffusion will also increase reaching a maximum at the target. Because it is held at this temperature for

presumably longer than it took to achieve it and cool from it and the maximum diffusion rate occurs at this temperature, it can be assumed that the majority of decarburization occurs at the temperature of interest.

1.6 Motivation

It is well known that decarburization occurs during heat treatment of most steels in a number of environments, and it is argued that the effect of atmospheric oxygen concentration should not affect the depth until very low partial pressures of oxygen, as discussed previously. However, the collaborator on this project, Canton Drop Forge, Canton, Ohio, wished to confirm the effect of reduced oxygen atmospheres, as present in the range of industrial forging exposures.

During drop forging of steels, billets are exposed to elevated temperatures to increase workability. This increased temperature is in the range of gross decarburization, and typically further processing must be utilized to eliminate its negative effects. During open drop forge operation, air flow and composition are not controlled, allowing exposure to a possible variety of gas compositions. Therefore, it is quite possible that the billets may be exposed to reduced oxygen air. The purpose of this investigation was to observe any affects reduced oxygen atmospheres (14% O₂ and 7% O₂, with a balance of nitrogen) would have during the heating of forged 300M alloy steel.

2. Experimental Procedure

2.1 Material

The material of this investigation was 300M alloy steel, a variation of 4340 alloy steel. A chemical analysis of the material is given in Table 2.1. Of note is the increase in silicon in 300M.^[15] The metal was supplied by Canton Drop Forge, Canton, Ohio in the form of three (3) 17.30 cm diameter x 1.27 cm discs and three (3) 17.30 cm diameter 2.54 cm discs. Sixteen (16) samples were cut from the center of a single 2.54 cm disc with approximate dimensions of 1.27 x 1.27 x 5.08 cm. Rockwell C tests in the as-received condition yielded a value of 27.5 HRC based on the average of three indentations.

The microstructure of an as-received sample is shown in Figure 2.1. The microstructure shows tempered martensite. Figure 2.2 displays the surface layer of the same sample to allow comparison of later laboratory decarburized samples. The microstructure is completely uniform up to the surface prior to decarburization, as would be expected in a sample cut from the middle of a disc.

2.2 Decarburizing Heat Treatment

2.2.1 Apparatus

A Eurotherm 2404 controller/set point programmer with a Lindberg tube furnace heating unit was used for all decarburizing and austenitizing. A combination of 0.635 cm (¼ in) and 2.54 cm copper piping connected the gas source (if applicable) and vacuum to the furnace, while 0.635 cm stainless steel piping connected the furnace exit piping. A schematic of the system set up is shown in Figure 2.3.

Standard size tanks at an initial pressure of approximately 13.1 MPa (1900 PSI) were used in this experiment. Compositions of 14% O₂ and 7% O₂ with a balance of nitrogen were used. The outlet pressure was controlled by a regulator directly connected to the tank nozzle. The gas source could be isolated by closing a ball valve located prior to the vacuum and furnace. Internal system pressure could also be equalized with the outside environment by opening the relief valve located just after the previously mentioned ball valve.

Table 2.1: Chemical analysis of the as-received 300M

Alloying Element	Percent (%)
Nickel	1.82
Molybdenum	0.41
Carbon	0.39
Phosphorus	0.007
Sulfur	0.001
Silicon	1.63
Titanium	0.01
Manganese	0.75
Tin	0.01
Chromium	0.75
Vanadium	0.07
Aluminum	0.04
Cobalt	0.02
Copper	0.17
Niobium	0.01
Iron	Balance

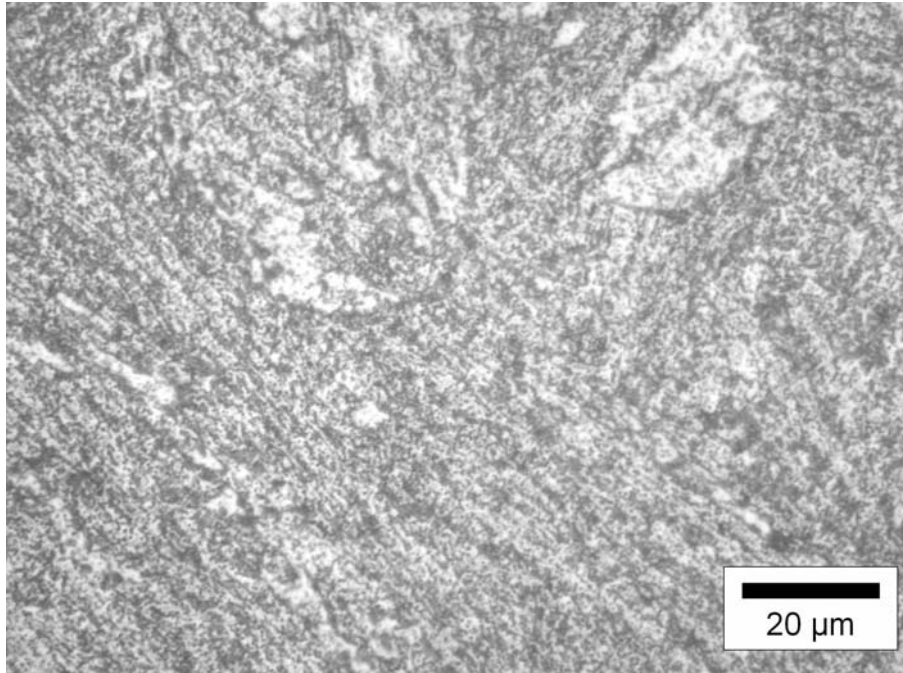


Figure 2.1: Microstructure of the as received alloy at 1000x.

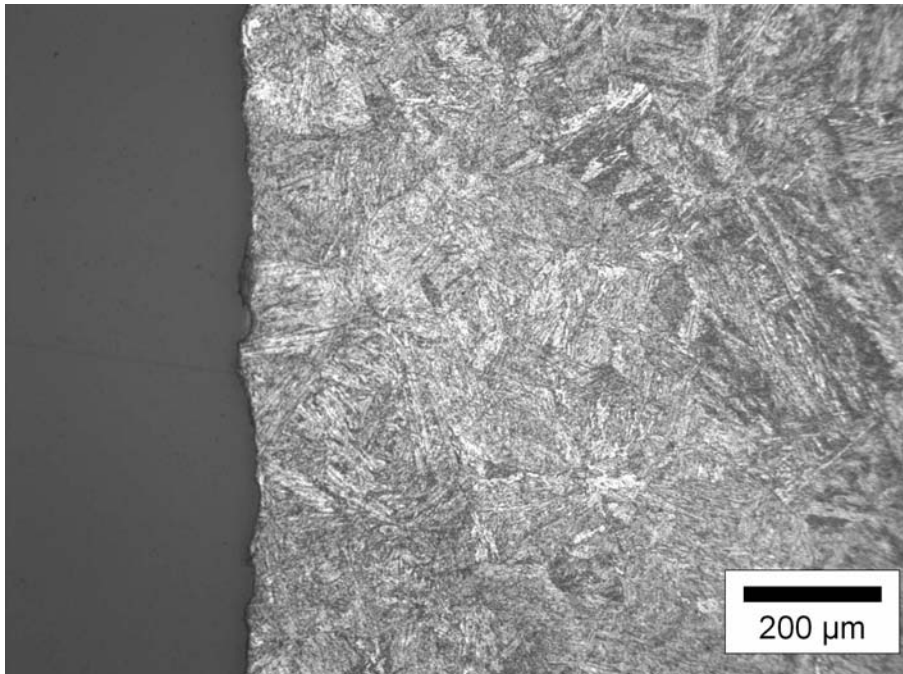


Figure 2.2: Surface microstructure of the as received alloy at 100x. Note the microstructure remains uniform up to the surface.

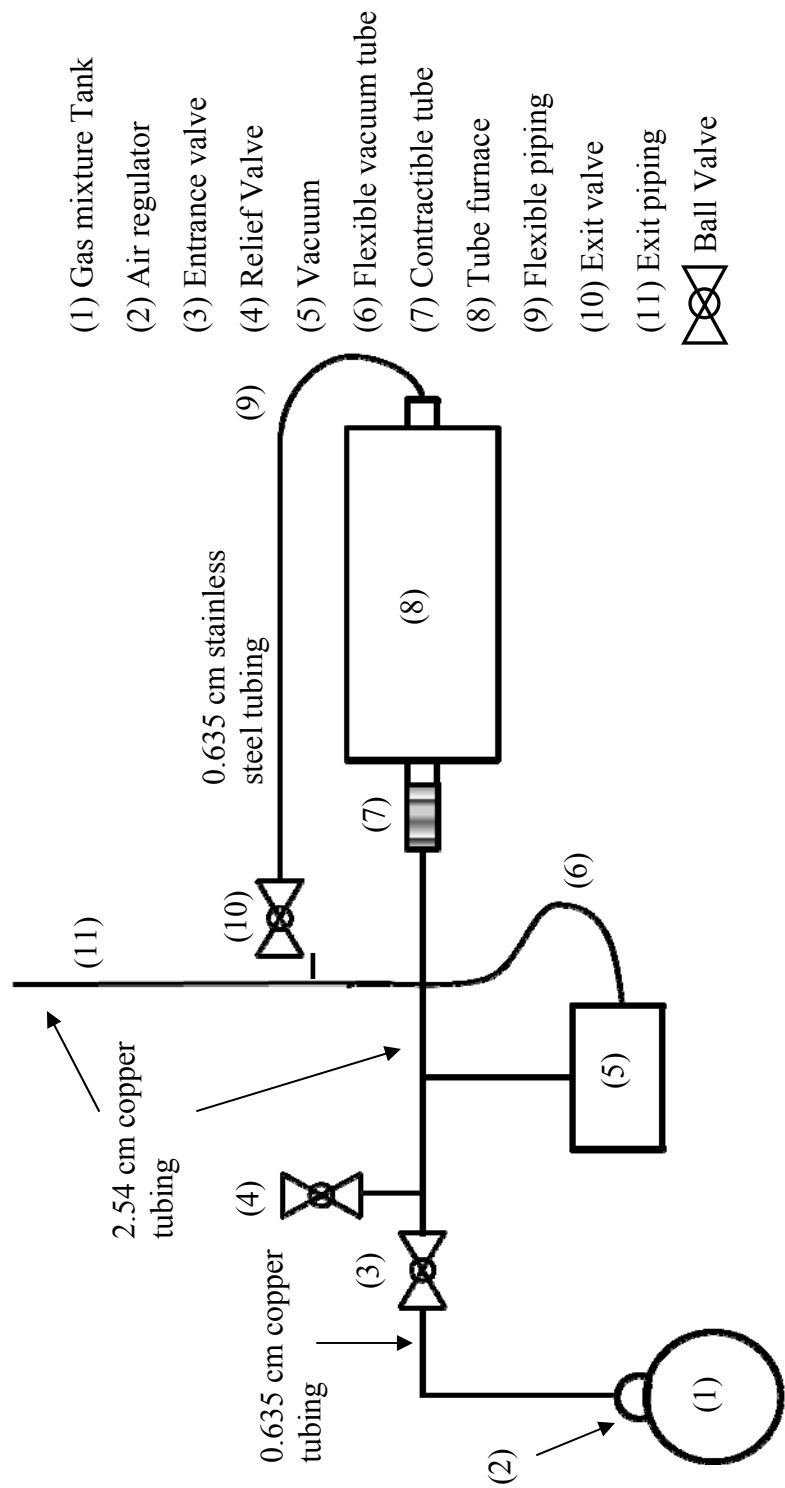


Figure 2.3: Schematic of the furnace apparatus used in the investigation

An Edwards RV8 Rotary Vane Pump, used to purge the system prior to heat treatments for gas mixture samples, was connected to the piping just prior to the entrance of the tube furnace. This pumped the air into the exit piping and had an internal valve which could be closed following initial purging.

The tube furnace consisted of the previously mentioned controller and heating unit, a fused quartz tube, and aluminum couplers to interface between the piping and tube. The fused quartz tube was a 5.08 cm diameter, 0.3 cm thick, 1.016 m long tube supplied by Technical Glass Products of Painesville Township, Ohio. The furnace was connected to the exit piping by 0.645 cm stainless steel piping. An additional ball valve (the “exit” valve) was located at the end of the stainless steel piping to allow complete isolation of the system with respect to the external environment, if closed in conjunction with the relief and entrance ball valves.

2.2.2 Heat Treatment Procedure

2.2.2.1 Furnace Setup and Programming

The Eurotherm 2404 may have up to 16 consecutive “steps” programmed, and repeat this program up 999 times without user interface. For the heat treatments in this investigation, only four steps were required:

- 1) A rate step in which the furnace and contents were heated up to the pre-programmed temperature at a designated rate ($^{\circ}\text{C} / \text{min}$). The parameters chosen for this were 800, 900, or 1000 $^{\circ}\text{C}$ at a rate of 8 $^{\circ}\text{C} / \text{minute}$.
- 2) A dwell step in which the furnace remained at the set temperature for a set length of time (two hours).
- 3) An additional rate step in which the furnace cooled to a set temperature (25 $^{\circ}\text{C}$) at a set rate. However, because the furnace did not have forced cooling, the cooling rate was limited to the rate of heat loss to the environment.
- 4) An end step, where the furnace either repeats the previous three steps, remains at the preset temperature from step 3 (if above room temperature), or applies no power. In this experiment, the last option was chosen although the samples were removed prior to attaining room temperature.

2.2.2.2 Heat Treatment Run-through

Samples were placed in the tube furnace on a ceramic sled following programming of the furnace to 800, 900, or 1000 °C. See Table 2.2 for all sample conditions. Samples 1, 2, and 3 required no gas mixture as they were heat treated in atmospheric conditions. The program for these samples was run and the samples were removed upon cooling to 300 °C. This removal temperature was chosen for the following reasons: 1) it lies within the $\alpha + \text{Fe}_3\text{C}$ region in the iron-carbon phase diagram, thus diffusion of carbon out of the sample is greatly reduced in comparison to the γ (austenite) region as discussed in section 1, and 2) at this temperature the diffusion rate, exponentially dependent on the temperature, is insignificant compared to that of the dwell temperatures. The samples were then cooled to room temperature in air outside of the furnace.

For the remaining samples, controlled atmospheres of oxygen and nitrogen were employed. Once samples were loaded into the furnace and the program begun, all valves were closed to completely isolate the system. The rotary pump then evacuated the furnace and the internal pump valve was closed, leaving the system in a reduced pressure. The gas mixture regulator was then opened until a pressure of 13.79 kPa was achieved. The entrance and exit valve were then opened to allow constant flow of the reduced oxygen gas over the sample through a majority of the remaining experiment duration. A pressure of the reduced oxygen was used to ensure a constant source of the gas was flowing over the sample. This pressure was maintained through the heating, dwell period, and the cooling step until 500 °C. At this temperature the exit valve, followed by the entrance valve, were closed. This left the system at a pressure of 2 psi and a reduced oxygen environment. The relief valve was then opened until the pressure reached that of the atmosphere and subsequently closed, but left the system in reduced oxygen for the remainder of the heat treatment. The flow was stopped at 500 °C to conserve gas; the vast majority of decarburization was believed to have occurred prior to this (mainly during the dwell period) and this gas conservation procedure was assumed to have little to no effect on the final outcome of any decarburization. Also, because from 500 °C to 300 °C the samples were still exposed to the reduced oxygen

Table 2.2: Decarburization conditions

Sample ID	Temperature of Initial Heat Treatment (°C)	Atmosphere (N₂ balance)
Sample 1	800	Air
Sample 2	900	Air
Sample 3	1000	Air
Sample 4	800	14 % O ₂
Sample 5	900	14 % O ₂
Sample 6	1000	14 % O ₂
Sample 7	800	7 % O ₂
Sample 8	900	7 % O ₂
Sample 9	1000	7 % O ₂
Control Sample	N/A	Air

concentrations but simply in stagnant gas, there should have been no significant effect. Equivalent to the atmospheric samples, reduced oxygen samples were removed at 300 °C for the two reasons previously discussed.

All samples were subsequently cut in a half. One half was used for decarburization analysis and the other for the hardening process (section 2.4).

2.3 Decarburization Analysis

Cross sections of the decarburized samples were cut approximately 1 cm from the edge to allow proper analysis of decarburization and microstructure. Samples were mounted in epoxy and subsequently polished and etched with 2% nital. A micrographic technique and software analysis were used to determine complete decarburization. Microhardness indentation was utilized to observe the total depth of decarburization. All estimates were in accordance with SAE Standard J419 - Methods of Measuring Decarburization and ASTM E 1077 - Standard Test Methods for Estimating the Depth of Decarburization of Steel Specimens.^{[16],[17]}

2.3.1 Complete Decarburization Software Analysis

Mounted samples were examined under a Leco Olympus PMG 3 microscope. Micrographs were taken of the surface layer of all samples at 50x, 100x, and 200x magnification. Attention was focused on the induced ferrite layer near the surface. This layer, known as the complete decarburization zone, occurs when the loss of carbon at the surface is at a concentration below the solubility limit of carbon in ferrite. This leaves a very characteristic pure ferrite zone indicative of near-total decarburization. Visual estimates were made as to this depth, however such method is problematic as the depth of this layer can vary drastically along the surface. As a more accurate method, AnalySIS[®] imaging software was utilized. The complete decarburization zones in the micrographs were isolated via a “set frame” command, allowing the user to conduct spectral analysis solely on this region. Figure 2.4 shows an example of this isolation step. The user may then set the threshold of these values, e.g. the range of contrast, which corresponds to ferrite. A phase analysis via the software was then conducted, producing a total area of ferrite. This area was then divided by the length of the region

in the micrograph to give an average complete decarburization depth. It should be noted that although there is also ferrite present beyond the complete decarburization depth, the contribution is negligible as most of it is averaged with pearlite to produce a gray tone.

2.3.2 Microhardness Indentation Method

To obtain the total depth of decarburization, that is, the distance from the surface to a location where the bulk carbon (hardness) is reached, 25g Vickers microhardness tests were conducted on all decarburized samples. A 25g load was selected as it is the lowest load allowed by ASTM Standard E 1077. It also produces the highest resolution of a hardness profile because indentations may be closer to one another than in larger load tests due to their relatively small size. To achieve hardness readings closer than the minimum of 2.5 diagonal lengths, closely spaced parallel transverses were used out to at least 420 μm as displayed in Figure 2.5. This figure also indicates the pattern generally used for all decarburized hardness tests. This pattern may be considered to be broken up into three regions:

- Region 1) Spacing of indents is 30 μm horizontally and 60 μm vertically (completely decarburized zone) or 50 μm (beyond the completely decarburized zone due to the immediate decrease in indent size)
- Region 2) Spacing of indents is 100 μm horizontally
- Region 3) Spacing of indents is 250 μm horizontally

The distance between indentations was thus in excess of the 2.5 diagonal length minimum in all cases.

To achieve increased accuracy in indentation dimensions, AnalySIS[®] software was once again used. Micrographs at a 200x magnification were taken and then zoomed in by a further 2x within the software. The software allowed the user to utilize a measurement tool, resulting in highly accurate diagonal lengths of indentations and therefore Vickers hardness values. This tool was also used to determine distances of the indentations from the surface. Values were then plotted as Vickers hardness vs. distance from the surface

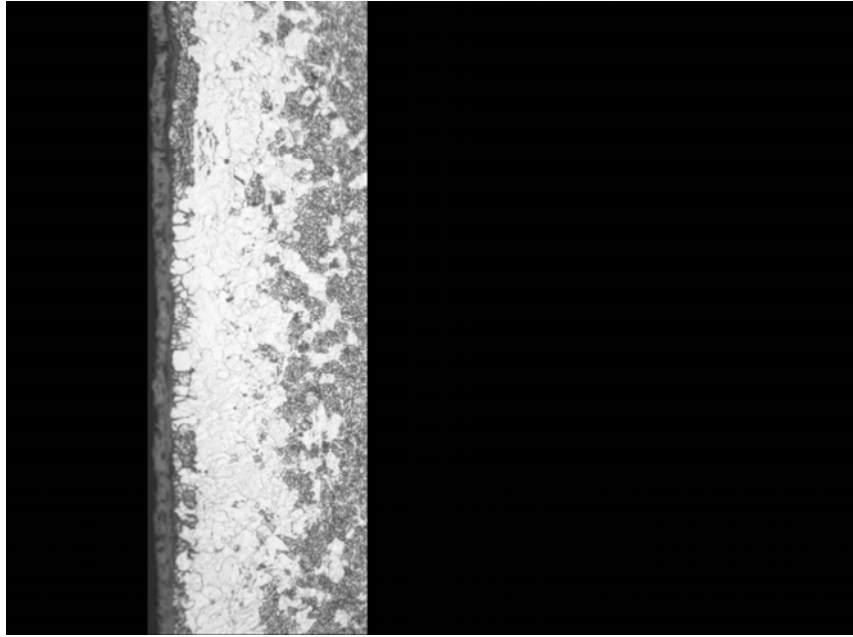


Figure 2.4: Example of ferrite (complete decarburization) isolation from a micrograph



Figure 2.5: An example indentation pattern used on the decarburized samples

(μm). Oxide layers were not included in distance measurements, but were measured separately.

2.4 Hardening of Samples

To emphasize hardness gradients due to decarburization, the remaining half of each sample was encapsulated in fused quartz at a pressure of 1.33×10^{-5} Pa (10^{-7} torr) and austenitized at 1000 °C for 30 minutes. The vacuum environment served to minimize further decarburization during austenitization in accordance with SAE J419. An as-received sample was also encapsulated and hardened to allow subsequent microhardness testing and observation of any decarburization which occurred during the austenitization. The capsules were then quenched in water and shattered under water, freeing the samples into the bath. Samples were subsequently mounted, polished, and microhardness tested. Due to the increase in hardness over the furnace / air cooled samples, a 50g Vickers hardness test was used. A similar pattern to Region one of Figure 2.5 was used with horizontal spacing of 30 micrometers and vertical spacing of 50 micrometers. This pattern was maintained out to approximately 1,000 micrometers, followed by at least three additional indentations of various horizontal spacing to ensure the bulk hardness had been obtained. All spacing of indentations was in excess of the 2.5 diagonal minimum as required by ASTM E 1077.

3. Results

3.1 Decarburized Samples

Due to the slow rate of furnace cooling, complete decarburization became very apparent prior to hardening of the samples. A distinct ferrite layer resulted at the surface region of the material, beyond which the carbon content increased until the bulk carbon content was obtained. The surface regions resulting from the individual decarburization processes are displayed in Figure 3.1 – Figure 3.9. It can be observed that the most dramatic increases in the complete decarburization (ferrite) region arise from an increase in temperature, as predicted. Ferrite is displayed as the white region; to the left of these regions are oxide layers of differing stoichiometries. As can be seen in these figures, the ferrite layer is not uniform in all cases and therefore makes precise determination of complete decarburization difficult. This area lacking homogeneity is likely a mixture of proeutectoid ferrite and pearlite, as it must possess a composition between the ferrite layer (less than .022% C) and the bulk. Thus, determining the true depth of ferrite is ultimately up to the investigator. Table 3.1 displays the ferrite depth as calculated via the AnalySIS[®] software method and by visual estimation. The difference between these readings arises from the fact the software method results in a depth which represents an average value, while the visual method estimates the furthest extent of the ferrite; ferrite regions which extend further into the bulk, abnormally, were ignored.

It should be noted that oxygen concentration had little effect on complete decarburization at all temperatures. However, it may be observed that the complete decarburization layer is significantly more solid in Sample 4 and 7 than in Sample 1. Also, at 800 °C there was a slight increase in complete decarburization depth as oxygen content decreased. This trend did not exist for the higher temperatures for neither the visual nor the software determination. Further, it appears as if a solid layer of ferrite did not fully develop in the 800 °C air sample (Sample 1). This indicates that the region still possessed carbon content above the solubility of iron.

Although prior to hardening complete decarburization is apparent, it does not represent the full extent of decarburization (“total” decarburization). Hardness profiles of samples in this condition may be found in Appendix B. Although these allow a rough

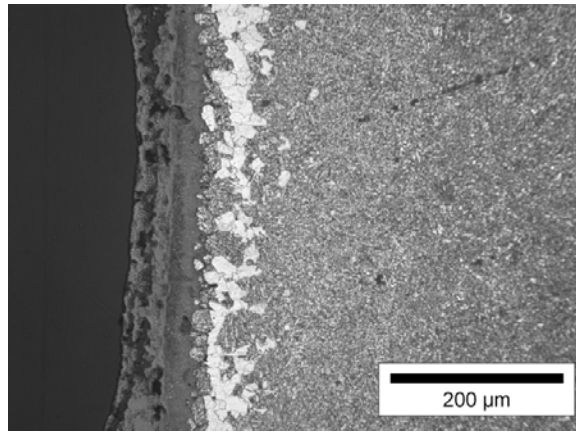


Figure 3.1: Sample 1 (800 °C in air) surface region following heat treatment

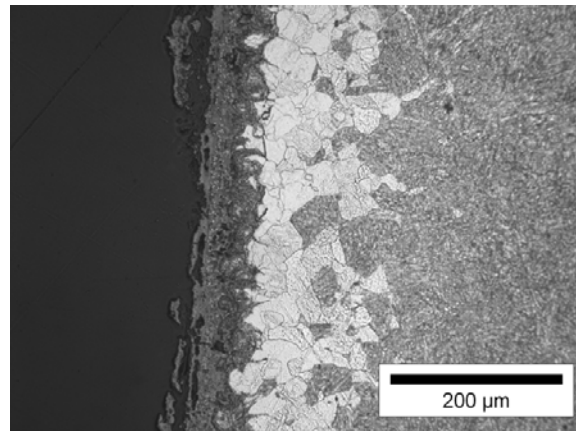


Figure 3.2: Sample 2 (900 °C in air) surface region following heat treatment, showing an increased ferrite region compared to 800 °C

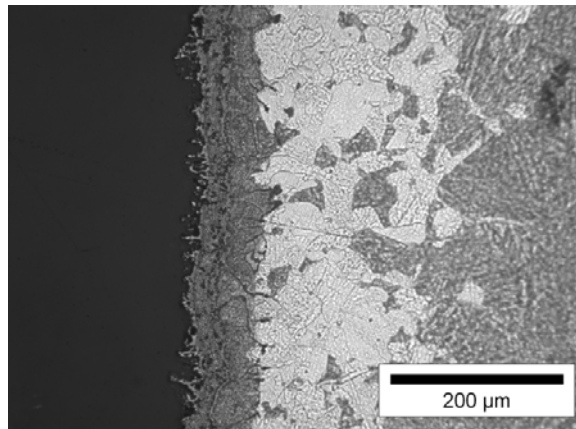


Figure 3.3: Sample 3 (1000 °C in air) surface region following heat treatment. Complete decarburization increased dramatically over Sample 1.

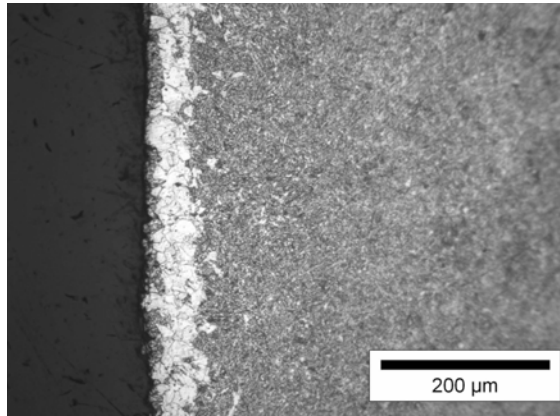


Figure 3.4: Sample 4 (800 °C in 14% O₂, balance nitrogen) surface region. The completely decarburized region increased from Sample 1. The oxide layer is not present in this photograph.

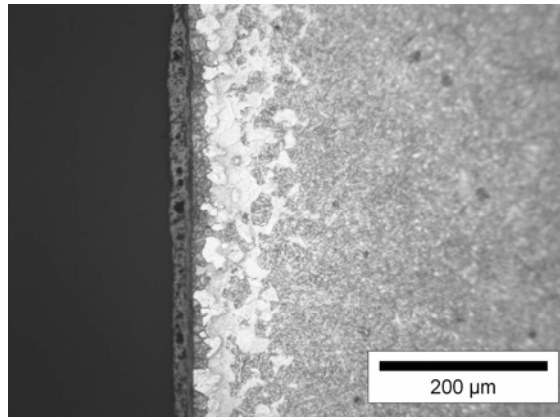


Figure 3.5: Sample 5 (900 °C in 14% O₂, balance nitrogen) surface region. The completely decarburized depth is very similar to Sample 2.

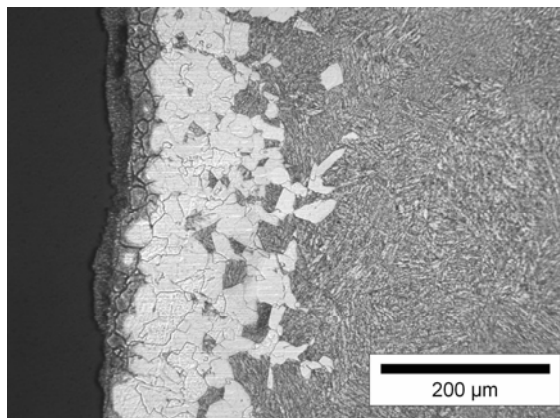


Figure 3.6: Sample 6 (1000 °C in 14% O₂, balance of nitrogen) surface region. Similar to Sample 5, little change occurred from the sample in air at the same temperature.

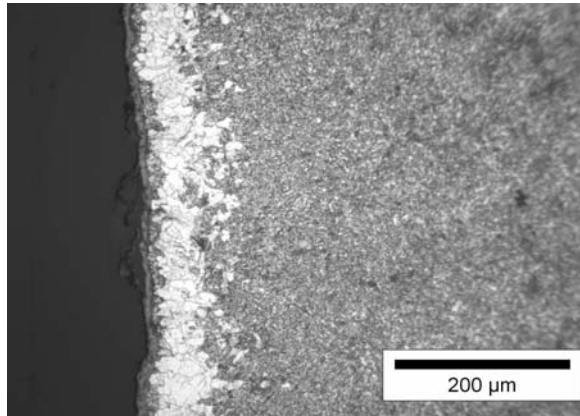


Figure 3.7: Sample 7 (800 °C in 7% O₂, balance nitrogen) surface region. An increase in the ferrite layer occurred in comparison to Sample 1, with a significantly reduced oxide layer.

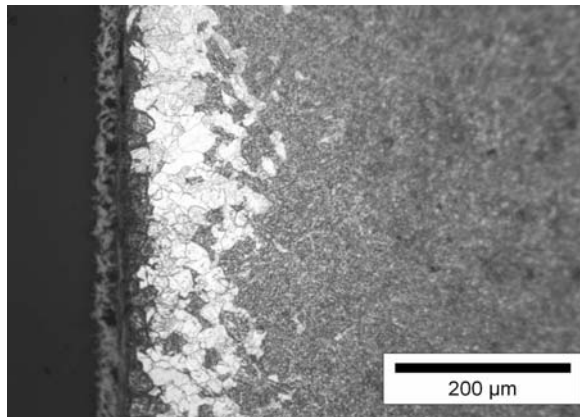


Figure 3.8: Sample 8 (900 °C in 7% O₂, nitrogen balance) surface region. The reduced oxygen atmosphere had little to no effect in comparison to temperature.

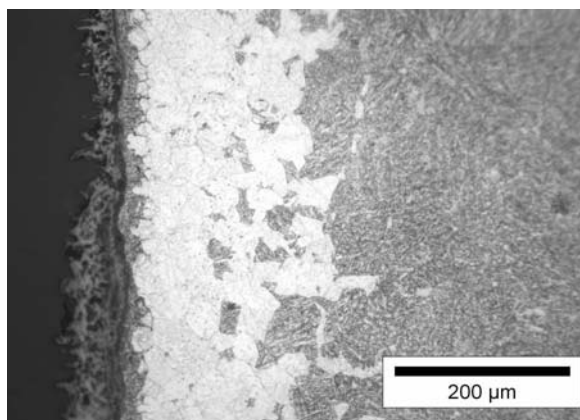


Figure 3.9: Sample 9 (1000 °C in 7% O₂, nitrogen balance) surface region. The ferrite region is approximately equal to the other two samples (3 and 6) heat treated at 1000 °C.

Table 3.1: Ferrite depths of decarburized samples

Sample	Software Method Depth (μm)	Visual Estimation Depth (μm)
1	40.3	46.3
2	94.7	136.1
3	158.2	208.8
4	44.5	52.3
5	84.6	103.4
6	138.6	185.0
7	56.9	59.9
8	85.4	117.7
9	169.0	198.6

estimate of the total decarburization depth, the hardness profile is greatly enhanced by austenitizing and quenching the samples.

Two representative microstructures are shown in Figure 3.10 and Figure 3.11. These micrographs show coarse pearlite formed from the slow cooling rate below the eutectoid point; thus the material was relatively soft prior to hardening. Additional micrographs may be found in Appendix C.

3.2 Oxide Layer Analysis

The total scale depth for each sample may be found in Table 3.2. For a given temperature, decreasing the oxygen concentration resulted in a reduced oxide layer with the exception of Sample 5 (900 °C in 14% O₂) to Sample 8 (900 °C in 7% O₂). The oxide layer was taken to be all material from the ferrite outward. As can be seen in Figure 3.12, some samples consisted of several distinct oxide layers differing in appearance. These layers presumably represent FeO and Fe₃O₄ or Fe₂O₃; however, they are nearly equal in depth and therefore do not represent the approximate 95:4:1 ratio typically present in scale.^[6] This ratio represents the relative depths of FeO:Fe₃O₄:Fe₂O₃ which form at elevated temperatures and is further explained in section 4.3. The layer of FeO is known to have very large defect mobilities in comparison to Fe₃O₄ or Fe₂O₃ and is believed to be what causes its large relative depth. As stated above, this ratio was clearly not present and therefore the oxide stoichiometries could not be determined from the relative thicknesses alone. The outer most oxide layer of Figure 3.12, known to be Fe₃O₄ or Fe₂O₃ due to its location in comparison to the metal and atmosphere, was extremely brittle and may be seen separating from the surface. Select samples also displayed a uniform phase immediately outside the ferrite region (Figure 3.13). Because ferrite contains nearly 0 wt% carbon and this region is present outside of that, it is assumed to be a form of scale.

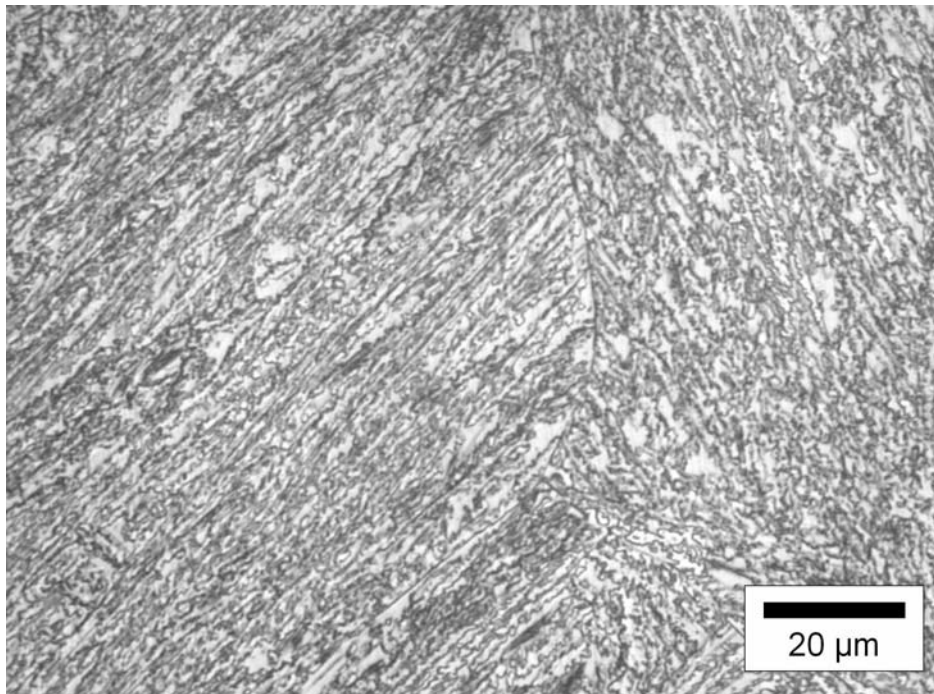


Figure 3.10: Microstructure of Sample 6 displaying oriented coarse pearlite taken at 1000x

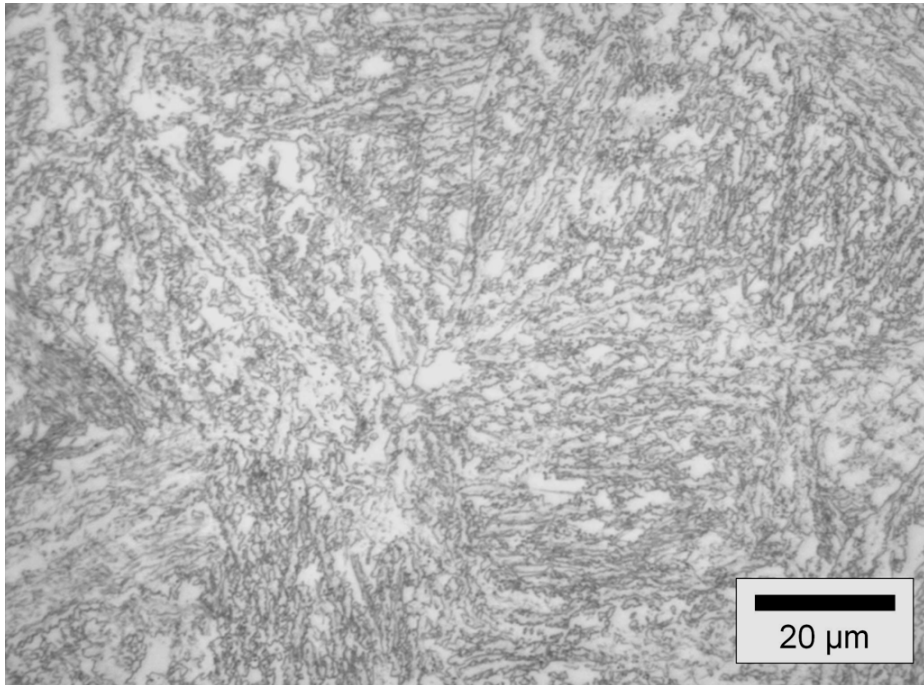


Figure 3.11: Microstructure of Sample 9 taken at 1000x

Table 3.2: Scale Depth

Sample	Scale (μm)
1	114.3
2	85.1
3	112.4
4	46.6
5	40.1
6	88.0
7	22.2
8	63.0
9	63.7

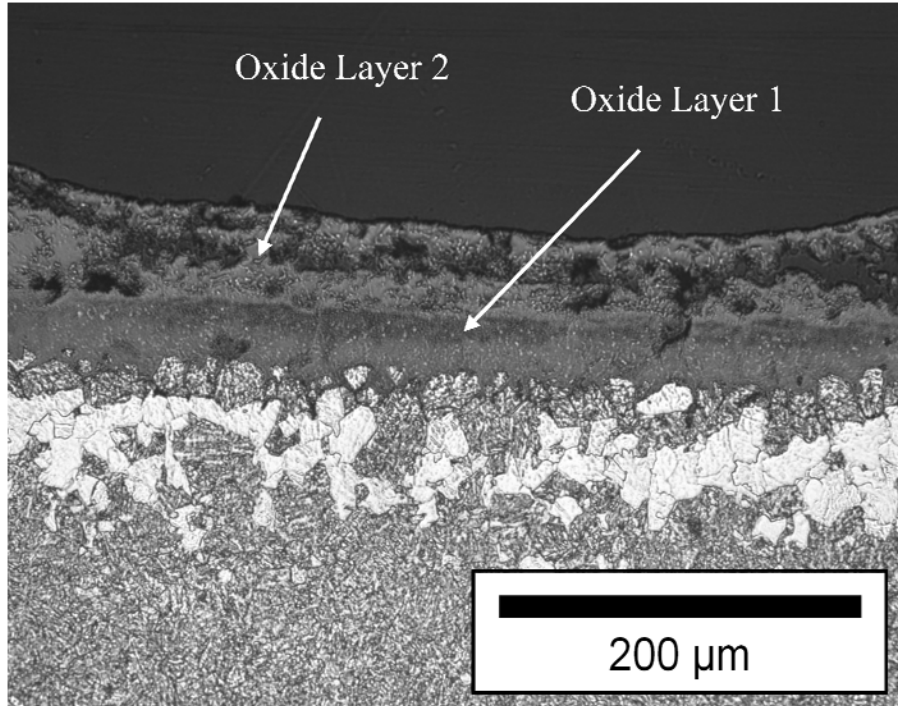


Figure 3.12: The oxide layers present in Sample 1

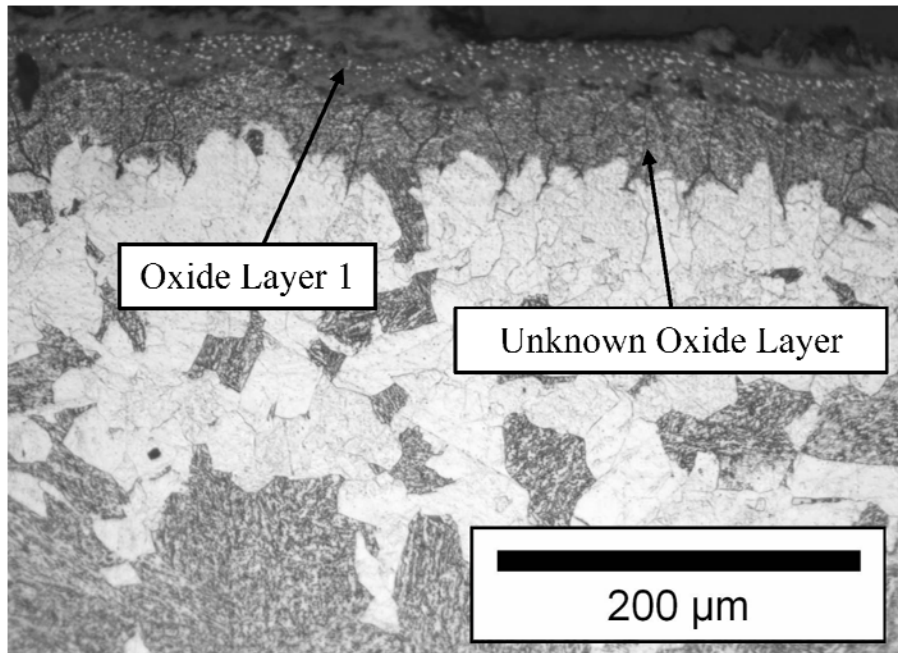


Figure 3.13: Sample consisting of an oxide of unknown stoichiometry

3.3 Hardened Samples

The hardening of samples was completed such that minimal further decarburization occurred in accordance with SAE J419. The resulting hardness profile of the hardened as-received sample is shown in Figure 3.14. It should be noted that the vertical label in this figure, HV.05, indicates a Vickers hardness test with a load of 50g (.05 kg). It can be concluded that no decarburization occurred in this sample as the hardness does not vary with depth.

The microstructure of a hardened sample revealed that the quenching from austenite resulted in a fully martensitic microstructure, as seen in Figure 3.15. Because this microstructure was located in the center of the sample, it served as a confirmation that the entire sample had transformed into austenite within the 30 minute austenitization period.

The hardness profiles of all hardened samples may be found in Figure 3.16 - Figure 3.24. Similar to the ferrite layer, temperature had the largest impact on total decarburization depth. The decarburized layer was considered to extend to the point in which the hardness was 90% of the difference between the surface and bulk:

$$HV_d = 0.9 \times (HV_B - HV_S) + HV_S \quad (21)$$

where HV_d is the hardness at the end of the decarburized layer, HV_B is the Vickers hardness of the bulk material, and HV_S is the Vickers hardness at the surface. The resulting total decarburized depths may be found in Table 3.3. For a given temperature, sample depths within 10% of one another were considered fairly similar; such results could be due to scatter. It may be observed that for a given temperature, samples possessing greater depths of ferrite did not necessarily display a greater total decarburization depth. In addition, Sample 5 (700 μm) had a reduced total decarburization depth compared to Sample 2 (825 μm) despite a reduced oxide layer in Sample 5.

A compilation of all relevant data – ferrite depth, scale depth, and total decarburization depth - for each sample may be found in Table 3.4.

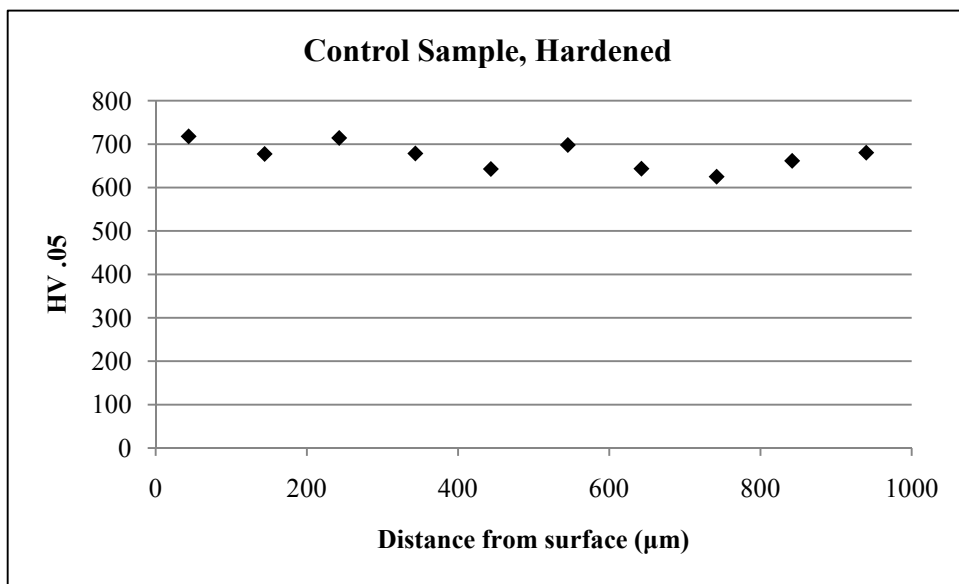


Figure 3.14: Hardness profile of the hardened as-received sample

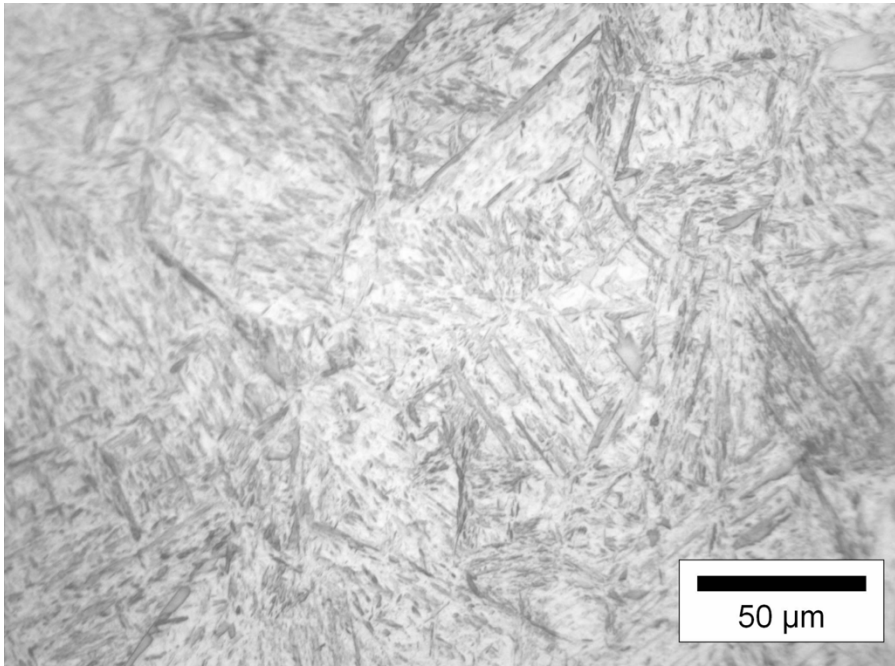


Figure 3.15: Representative microstructure of a hardened sample

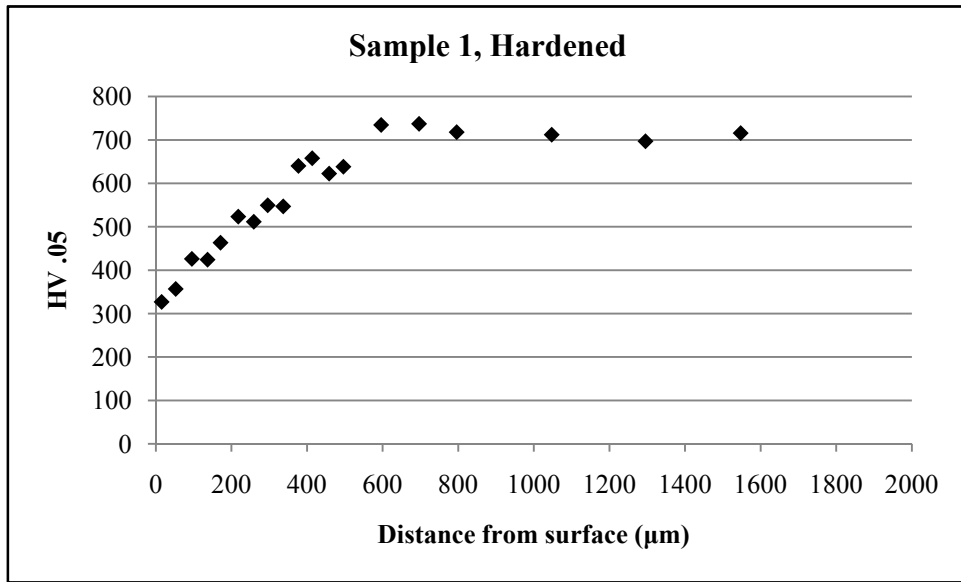


Figure 3.16: Hardness profile of Sample 1

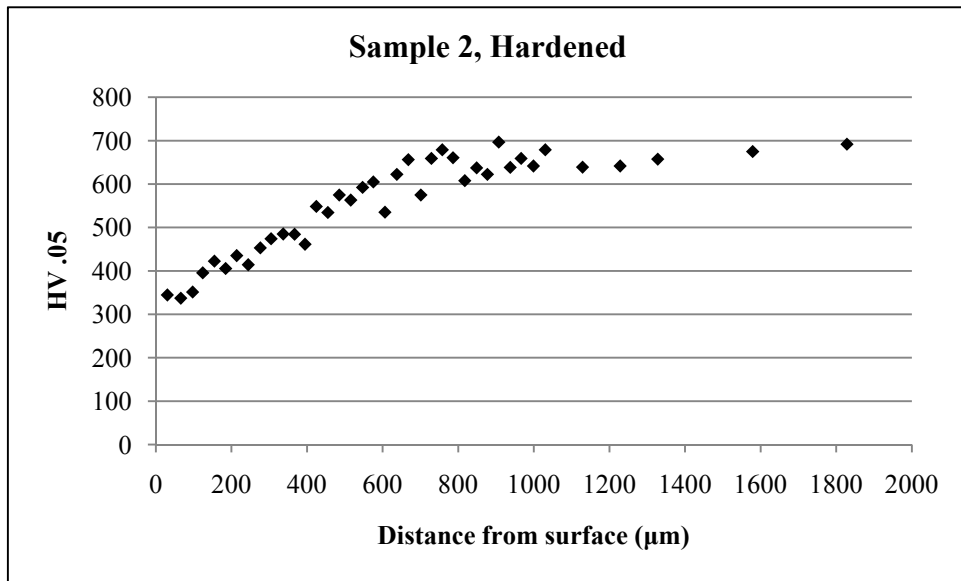


Figure 3.17: Hardness profile of Sample 2

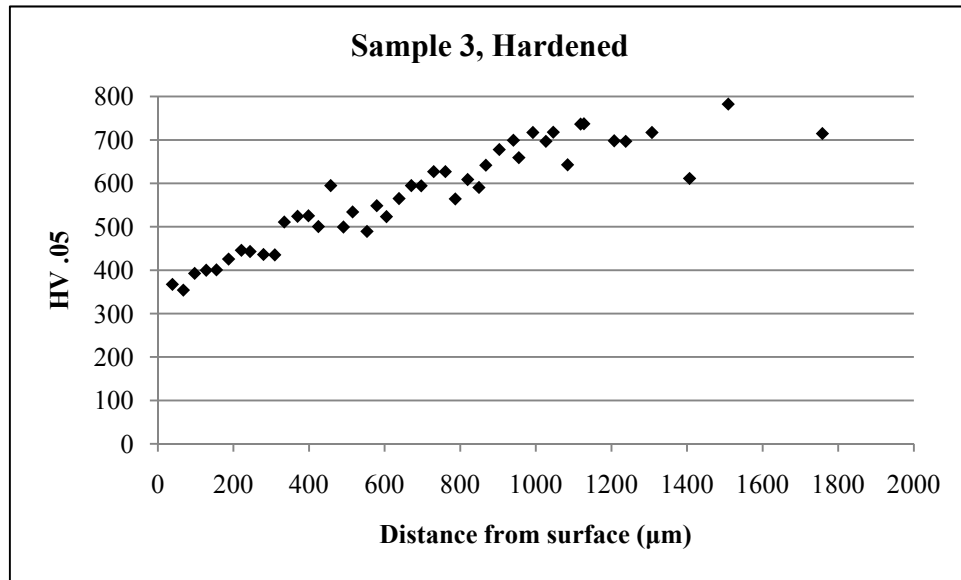


Figure 3.18: Hardness profile of Sample 3

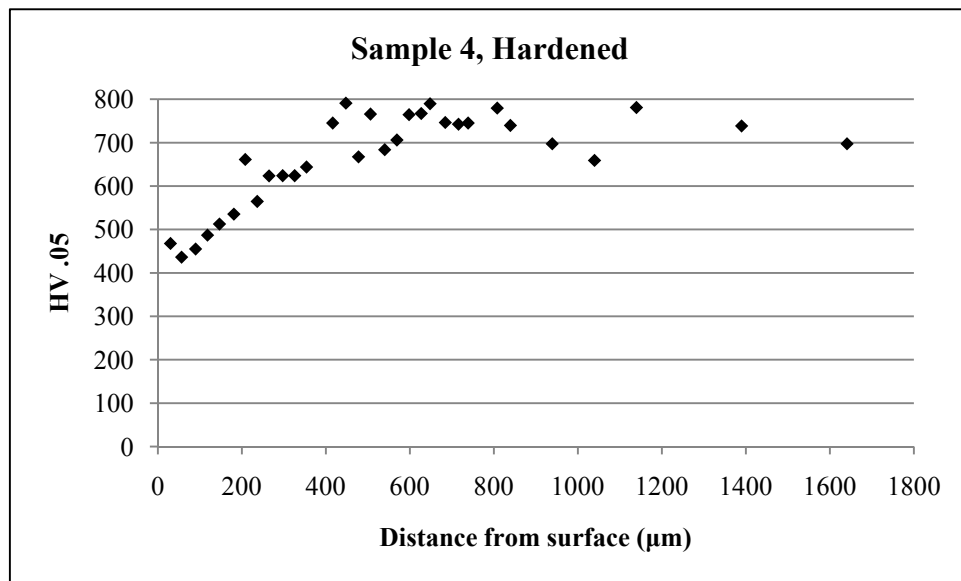


Figure 3.19: Hardness profile of Sample 4

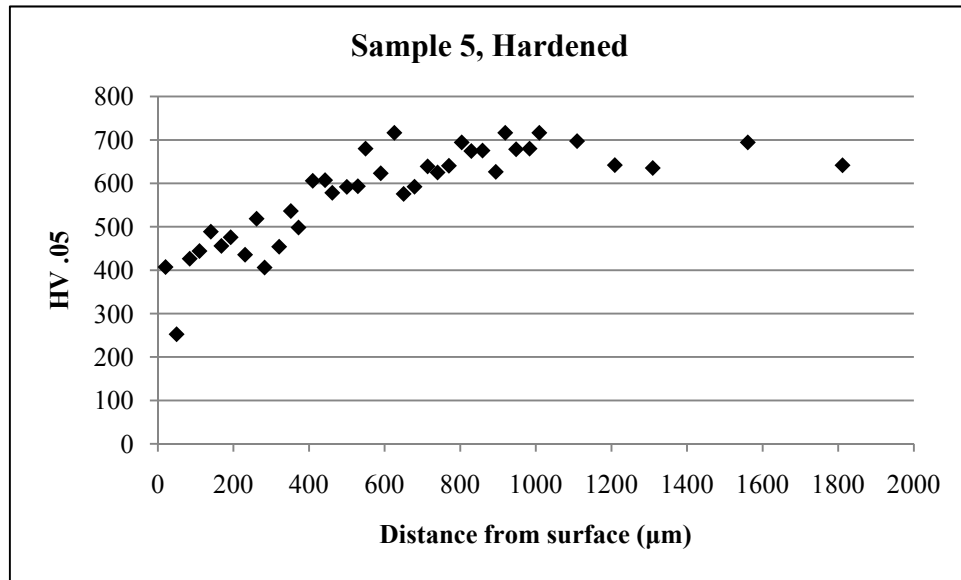


Figure 3.20: Hardness profile of Sample 5

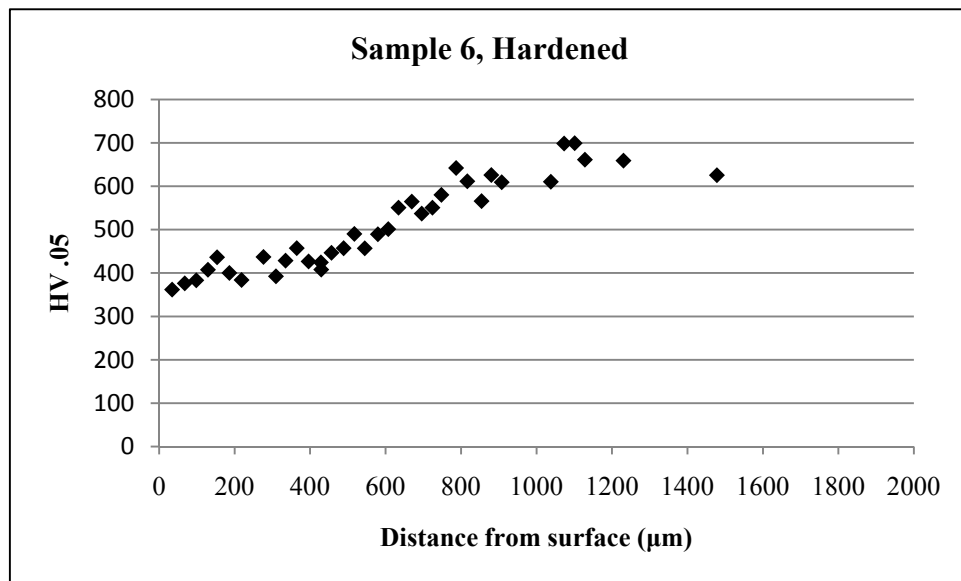


Figure 3.21: Hardness profile of Sample 6

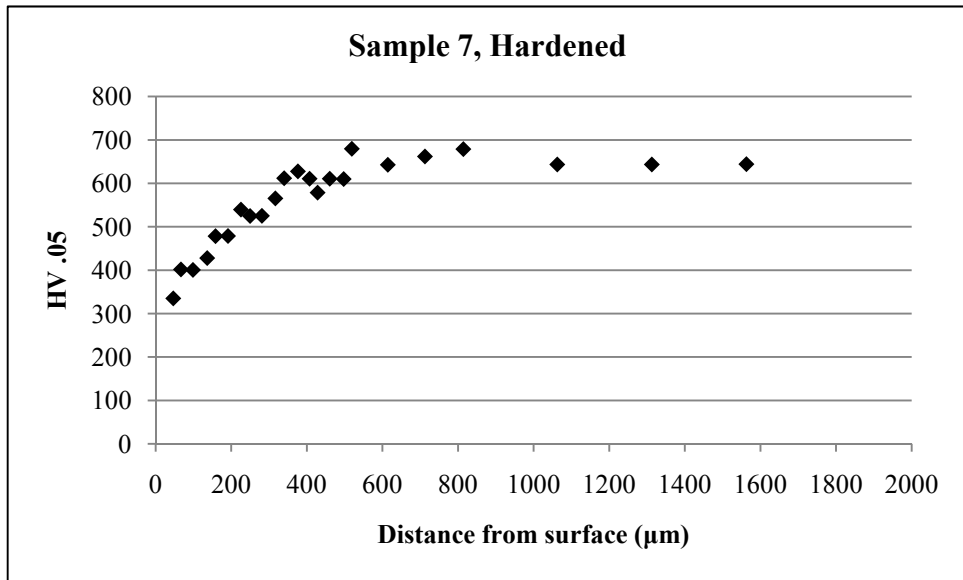


Figure 3.22: Hardness profile of Sample 7

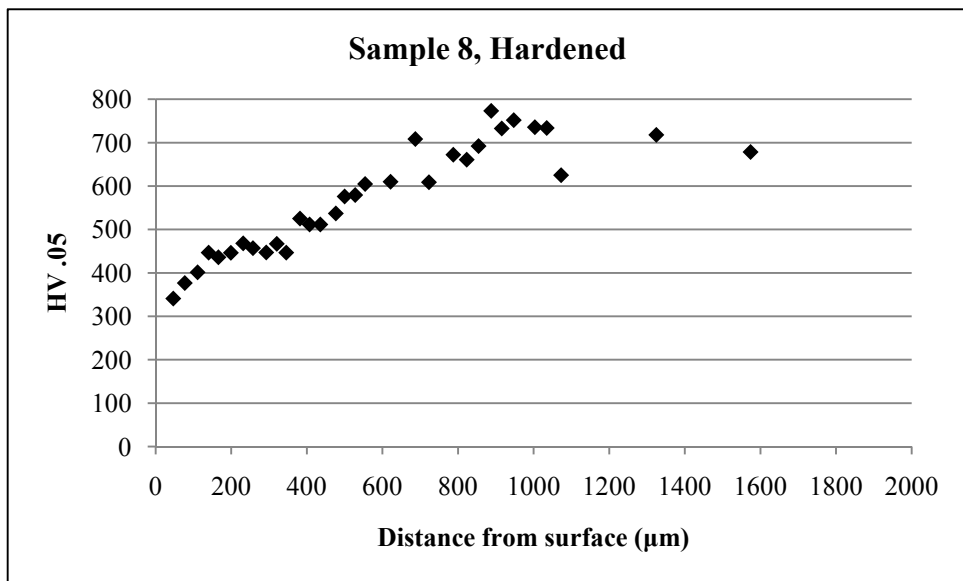


Figure 3.23: Hardness profile of Sample 8

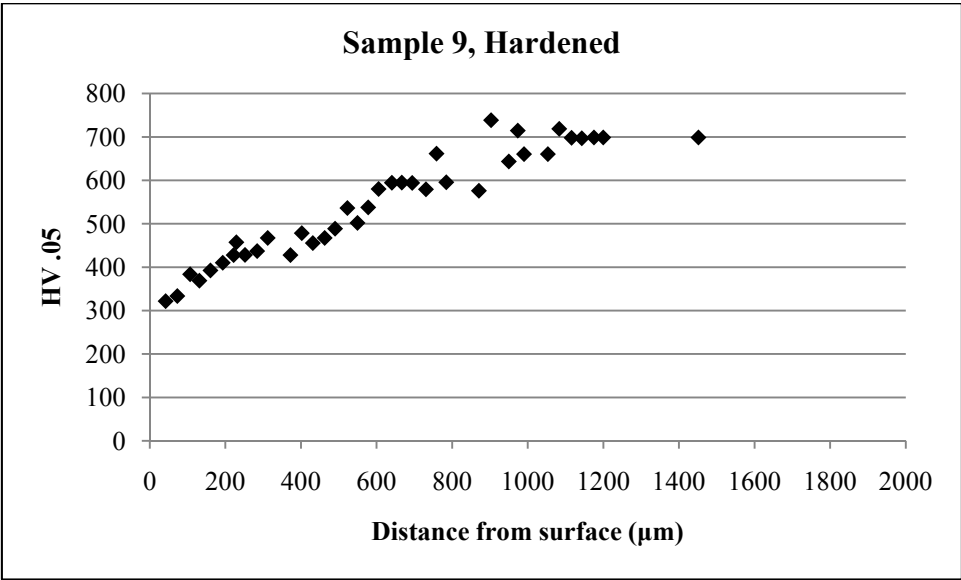


Figure 3.24: Hardness profile of Sample 9

Table 3.3: Total decarburization depth of the samples

Sample	Surface Hardness	Bulk Hardness	Decarburization Depth Hardness	Total Decarburization Depth (μm)
1	327	710	671.7	500
2	345	675	642	825
3	367	710	675.7	995
4	436	740	709.6	530
5	407	680	652.7	700
6	362	650	621.2	1005
7	335	662	629.3	480
8	341	710	673.1	760
9	322	700	662.2	900

Table 3.4: Resulting characteristic depths by sample

Sample	Visual Estimation of Ferrite Depth (μm)	Scale (μm)	Total Decarburization Depth (μm)
1	46	114	500
2	136	85	825
3	209	112	995
4	52	47	530
5	103	40	700
6	185	88	1005
7	60	22	480
8	118	63	760
9	199	64	900

4. Discussion

4.1 Comparison of Results to Estimates

The difference between the estimated total depth of decarburization in air (Table 1.1) and the actual total depth of decarburization (Table 3.3) is worthy of discussion. It is obvious that the models consistently underestimated the decarburization that occurred in air. According to Equation (11), this could be due to the scale which formed during the heat treatment. However, as seen in Table 4.1, after enforcing the complementary error function scale factor of Equation (11), the estimated decarburized depth is reduced due to the formation of the scale. The k_c factors (Appendix D) were calculated using the scale depths observed for each sample and Equation (12). This factor could not be incorporated prior to testing because the parabolic rate constant for oxidation, and therefore the depth of scale, was required. Such values were not discovered in literature searches for the particular alloy under investigation. Table 4.1 also estimates the depth of total decarburization via Equation (11) for the reduced oxygen atmospheres. The effect of such atmospheres is incorporated into the rate constant for oxidation. It is believed that any effect the oxygen concentration has will alter the decarburization through the modification of the scale depth or chemical activity of the oxide-steel interface. Decarburization occurs mainly through the combination of an oxide and carbon in the steel and there is very little direct combination of gaseous oxygen and this carbon. Therefore the estimates of decarburization depth under these conditions through Equation (10) are not altered from estimates in air; only through consideration of scale (Equation (11)) are the oxygen concentration effects observed.

There are several factors which may contribute to the measured total decarburization depth exceeding predictions. One such explanation involves the diffusion of carbon from the specimen at temperatures below the phase transformation to the FCC structure. Although at temperatures below approximately 727 °C the layer of ferrite which forms is thought to severely restrict further decarburization, in long durations and at several hundred degrees this may allow considerable carbon loss. Consider a eutectoid steel below 727 °C. The structure is body centered cubic (BCC) and therefore the atomic packing factor is below that of the FCC structure, increasing the

Table 4.1: Incorporation of scale on total decarburization depths

Sample	Estimate of Total Depth Effected* (μm)	Scale (μm)	Estimated Total Decarburization Depth (μm)	Measured Total Decarburization Depth (μm)
1	290	114	176	500
2	515	85	430	825
3	916	112	804	995
4	255	47	208	530
5	495	40	455	700
6	904	88	816	1005
7	245	22	223	480
8	505	63	442	760
9	895	64	832	900

*Total Depth Effected was calculated from Equation (11), which calculates the depth of the scale and the total decarburization

probability of carbon to successfully diffuse through the bulk. This alters the temperature independent pre-exponential factor and activation energy of Equation (7) to:

$$D = 6.2 \times 10^{-7} \exp\left(-\frac{80,000}{8.314T}\right) \quad (22)$$

At a temperature of 700 °C, this yields a diffusion constant of 3.13×10^{-11} m²/s, a value implying diffusion occurs more rapidly than carbon in austenite at 1000 °C (1.94×10^{-11} m²/s). Although the layers of ferrite, and possibly other phases, slow the decarburization process, such an effect could certainly contribute additional carbon loss. Because the samples were in the furnace during the heating process, they were exposed to the entire range of temperatures for the entire duration. The heating process varied from two hours to three hours depending on the dwelling temperature, allowing considerable exposure. They were also exposed to these diffusion conditions during cooling, which typically took longer than heating. Further, there is the possibility of decarburization via grain boundary diffusion. Although the layer of ferrite formed at the surface may impede bulk diffusion, grain boundaries within this ferrite may allow such a process.

Alternatively, if the layer of ferrite developed during heating does prevent significant decarburization, it is still possible that the exposure to temperatures in the $\alpha + \gamma$ and γ region would allow the additional decarburization observed. Although exposure times in this temperature range prior to the dwell temperature were limited, decarburization certainly occurred. The estimated decarburization depths did not take this into consideration. One would expect the measured total decarburization depth and estimated value to differ more greatly as temperature increased due to the increase in time to reach higher temperatures. This was not observed in the results, however, and thus the disparity between the predictions and measurements could be a combination of the above.

4.2 Proposed Prediction Model

In a format similar to Equation (14), an equation has been produced which relates the time, temperature, and oxygen concentration to the depth of total decarburization in the temperature range of 800 - 1000 °C. This equation is limited to the conditions and material of this investigation, as samples were exposed to heating and cooling through a range of temperatures. Figure 4.1 through Figure 4.3 display plots by atmospheric condition of the natural log of the total decarburization depth vs. the reciprocal temperature in Kelvin to allow the application of best fit Arrhenius equations:

$$d = 43400 \exp\left(-\frac{4700}{T}\right) \quad (23)$$

$$d = 29700 \exp\left(-\frac{4300}{T}\right) \quad (24)$$

$$d = 28400 \exp\left(-\frac{4300}{T}\right) \quad (25)$$

which correspond to air (21% O₂), 14% O₂, and 7% O₂, respectively. It can be seen that the pre-exponential temperature independent constant and the activation energy (which has been divided by the gas constant) of each of these differs slightly, although Equations (24) and (25) do have very similar values. As can be seen in Figure 4.4 and Figure 4.5, these values were plotted vs. oxygen content and a best fit polynomial was applied to both:

$$\frac{Q_A}{R} = 4.08p^2 - 85.8p + 4700 \quad (26)$$

$$d_0 = 126.5p^2 - 2470p + 39500 \quad (27)$$

where p is the atmospheric oxygen concentration, in percent.

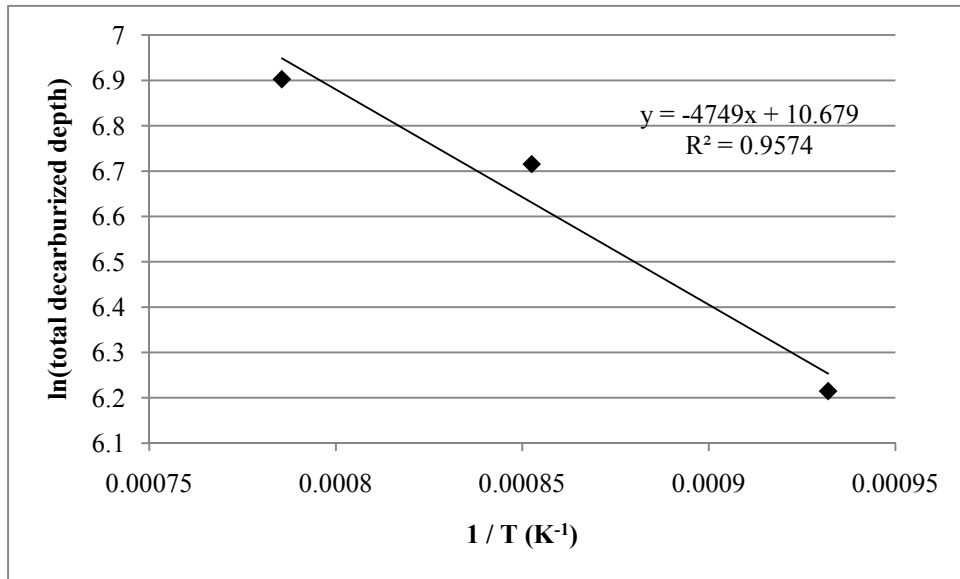


Figure 4.1: Natural log of total decarburization depth vs. reciprocal temperature to allow creation of an Arrhenius equation for 21% O₂

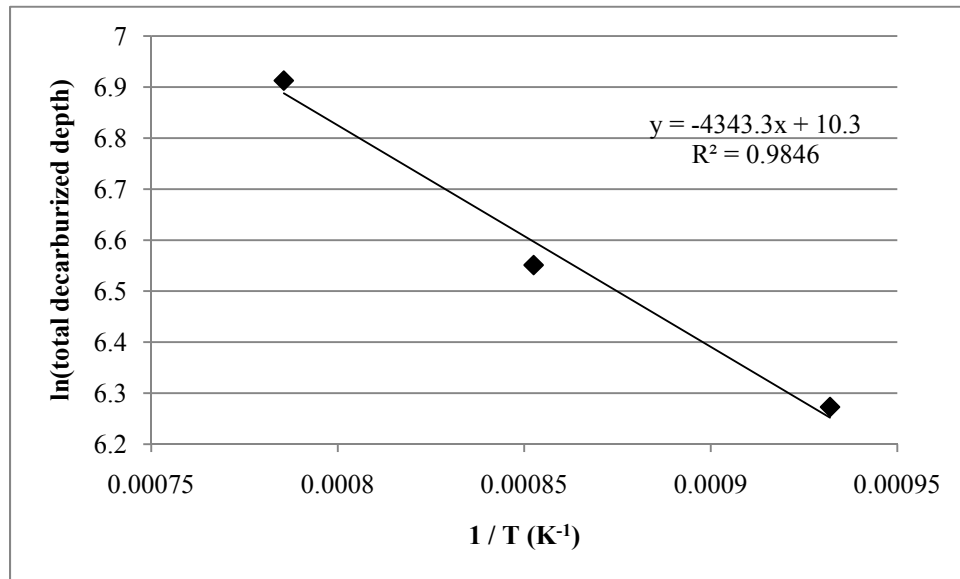


Figure 4.2: Natural log of total decarburization depth vs. reciprocal temperature to allow creation of an Arrhenius equation for 14% O₂

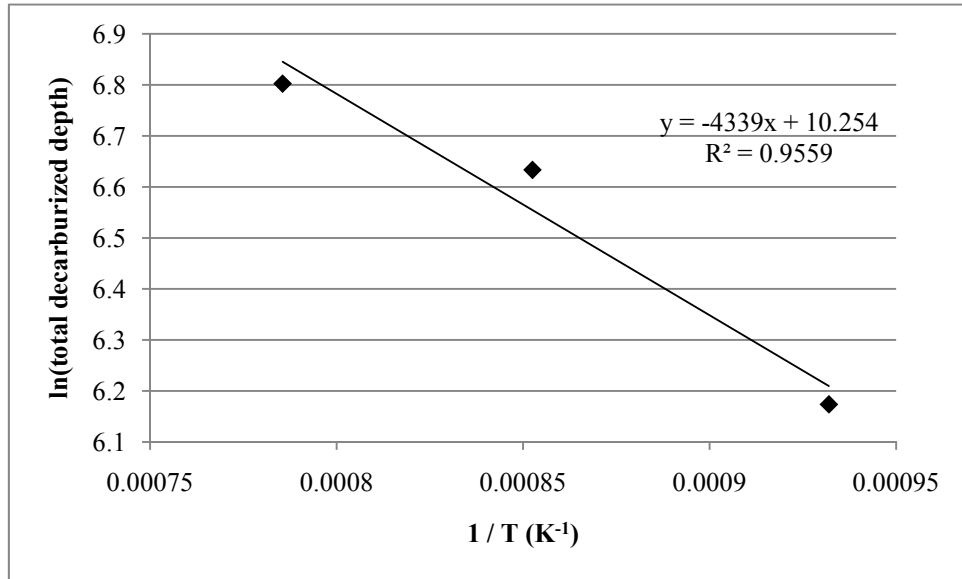


Figure 4.3: Natural log of total decarburization depth vs. reciprocal temperature to allow creation of an Arrhenius equation for 7% O₂

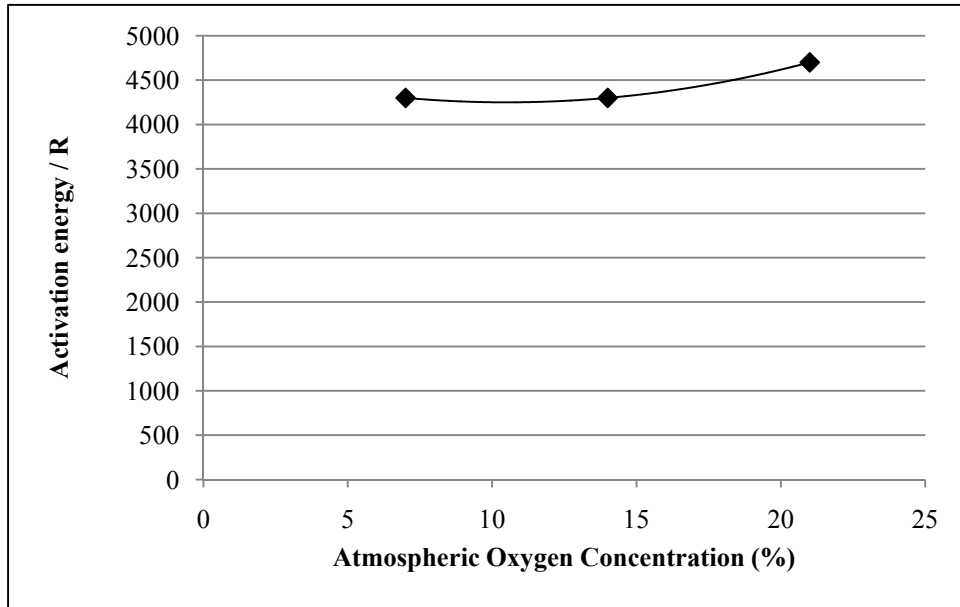


Figure 4.4: Plot of activation energies vs. oxygen concentrations to allow creation of a best fit polynomial

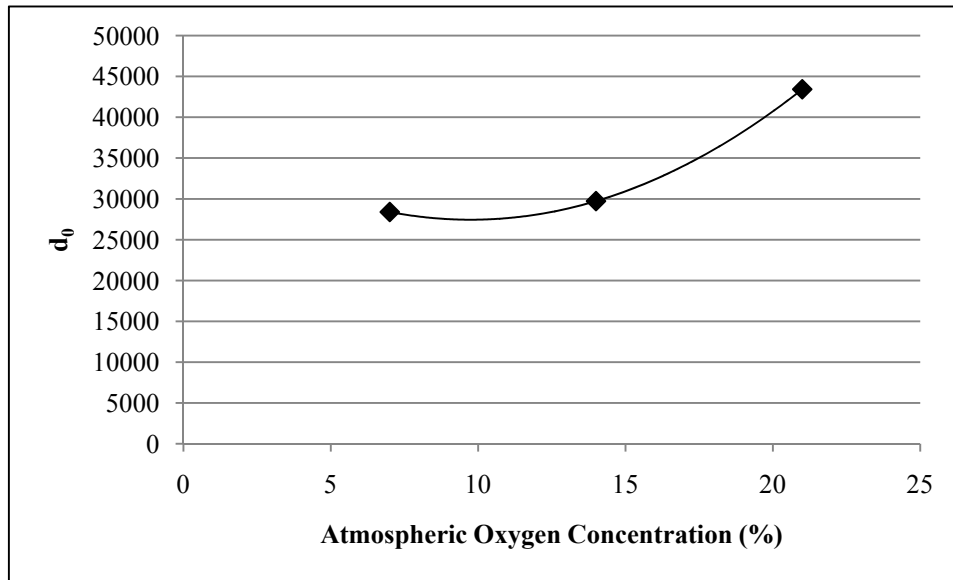


Figure 4.5: Plot of the pre-exponential constant vs. oxygen concentration to allow creation of a best fit polynomial

As mentioned above, it should be noted that both the activation energy and pre-exponential coefficients of the 14% O₂ and 7% O₂ are very similar. This may be due to either the flow of gas present in these samples that is absent in the air samples, or simply a sudden decrease in these values below the oxygen content of air. As seen below, it did not alter the prediction capability of the algorithm created.

Combining Equation (26) and (27), the total decarburization depth may be predicted by Equation (28):

$$d = (126.5p^2 - 2470p + 39500) \times \exp\left(-\frac{4.08p^2 - 85.8p + 4700}{T}\right) \quad (28)$$

where d is in micrometers (m⁻⁶). Table 4.2 allows comparison of the predicted depths of decarburization from Equation (28) and the measured depth. This table also indicates that all estimations are within 10% of the true depth.

The pre exponential constant of Equation (28) includes the contribution of time. It is well known that diffusion is related to time by the one-half power, and thus in a manner similar to Equation (14), Equation (28) may be rewritten:

$$d = (1.491p^2 - 29.1p + 466) \times t^{\frac{1}{2}} \times \exp\left(-\frac{4.08p^2 - 85.8p + 4700}{T}\right) \quad (29)$$

where the pre-exponential coefficient (no longer a constant) of Equation (28) was divided by the time of this investigation to the one-half power, or $7200^{1/2} = 84.9 \text{ s}^{1/2}$.

Table 4.2: Comparison of predicted total decarburization from Equation (28) and measured depths

Sample	Atmospheric Oxygen Concentration (%)	Temperature (K)	Estimated Depth (μm)	Measured Depth (μm)	Percent Difference
1	21	1073	545	500	9.00%
2	21	1173	791	825	-4.12%
3	21	1273	1084	995	8.94%
4	14	1073	541	575	-5.25%
5	14	1173	761	700	8.71%
6	14	1273	1015	1005	-1.00%
7	7	1073	517	480	7.71%
8	7	1173	727	760	-4.32%
9	7	1273	970	900	7.78%

4.3 The Oxidation Process

The fact that all samples were exposed to the full range of temperatures throughout each heat treatment cycle certainly complicated the oxide layer formed on the surface. Below 570 °C, FeO (wustite) will not form regardless of the oxygen weight percentage; $\alpha\text{-Fe} + \text{Fe}_3\text{O}_4$, $\text{Fe}_2\text{O}_3 + \text{Fe}_3\text{O}_4$, or $\text{O}_2 + \text{Fe}_2\text{O}_3$ will form in order of increasing oxygen content (see Figure 4.6 for the iron-oxygen phase diagram). It can be assumed that one of these pairs formed on the surface of the samples in this low temperature range. Above 570 °C FeO will begin to form if the scale formed is below approximately 27.5 oxygen wt%. The complication arises from when the FeO, the least rich oxide, forms next to steel where the scale had formed below 570 °C. Therefore this region directly next to the steel at temperatures above 570 °C becomes a mixture of FeO and the oxide stoichiometry formed previously. However, detailed analysis of the scale was outside the scope of this investigation, which strictly focused on the effect reduced oxygen had on decarburization depth.

Referring to Figure 3.1 through Figure 3.3 and Table 3.2, it can be observed that the samples decarburized in air had a fairly constant oxide depth regardless of temperature, yet scaling rate is predicted to follow an Arrhenius equation. However, Sample 1 shows very distinct oxide layers while Sample 3 shows significantly less variation and what appear to be grain boundaries within the nearest oxide layer, presumably FeO composing the majority of it. These grain boundaries would allow carbon monoxide to travel through the scale with ease compared to the solid oxide layer in Sample 1. This would ultimately lead to the greater depth of total decarburization observed in Sample 3 (Table 3.4), despite similarities in scale depth. Sample 2 shows a somewhat intermediate scale appearance between the two.

The appearance of scale in Sample 1 is worthy of discussion. It can be seen in Figure 3.12 that the two distinct oxide layers formed are very close to being equal in depth. However, as cited in section 3.2, the thickness ratio of $\text{FeO}:\text{Fe}_3\text{O}_4:\text{Fe}_2\text{O}_3$ is expected to be roughly 95:4:1. This ratio was predicted for 1000 °C, while Sample 1 was decarburized at 800 °C. Moreover, Figure 4.7 displays the scale of Sample 3, which was decarburized at 1000 °C in air and would be expected to exhibit this ratio. As

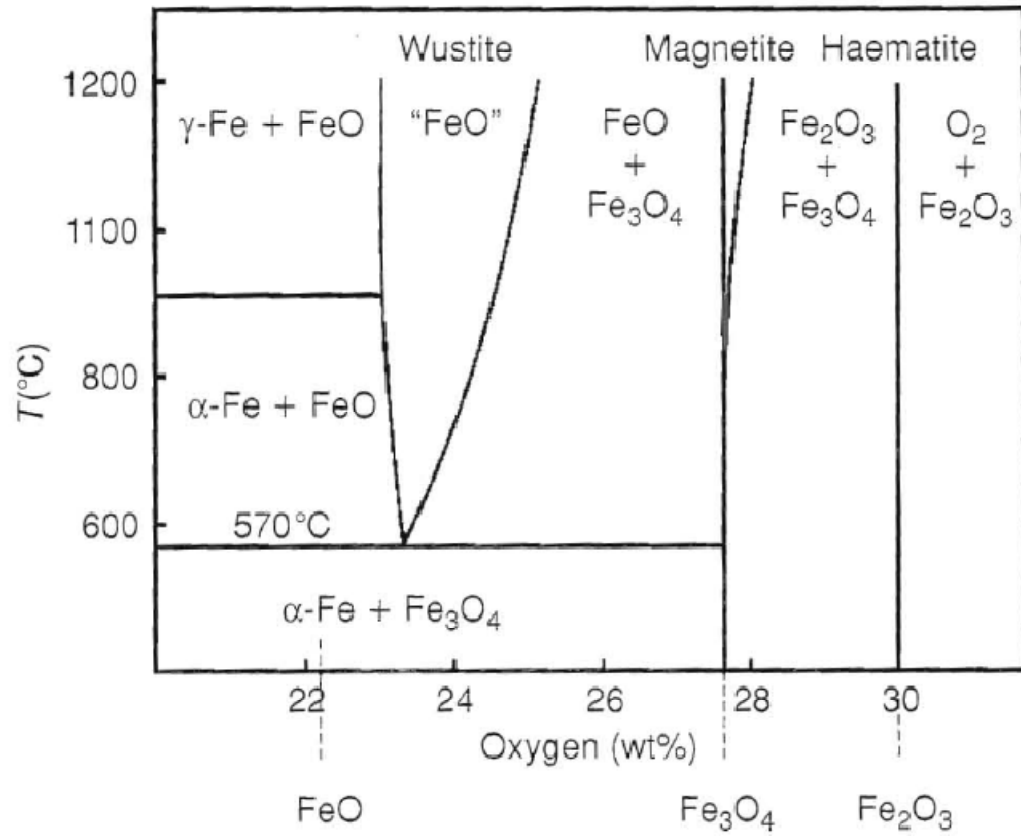


Figure 4.6: The iron-oxygen phase diagram. Reproduced from N. Birks., G. H. Meier, and F. S. Pettit. *Introduction to the High-temperature Oxidation of Metals*. 2nd ed. New York: Cambridge University Press, 2006. Print.

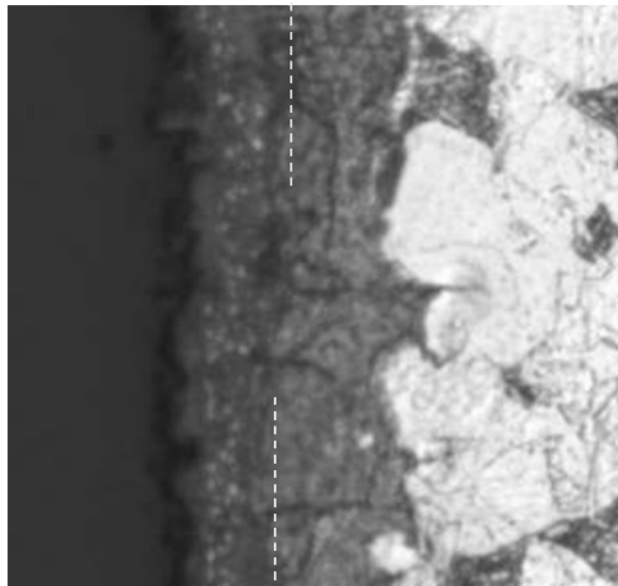


Figure 4.7: The two oxide layers formed on the surface of Sample 3. Taken at 200x.

indicated by the white line representing the interface of the oxide layers, it is evident that this ratio is not present. The ratio is approximately 2:1, far from the literature prediction. In addition, only two phases are present. It is believed that Fe_2O_3 is not present as its contribution to thickness would be minimal. The phase directly to the left of the white colored ferrite is believed to be FeO as iron is readily available to oxidize from the ferrite, and to the left of that is Fe_3O_4 , the next richest oxide. Such an explanation may be applied to the “unknown” oxide layer in Figure 3.13. Because there are two distinct layers, the layer next to the steel has a readily available supply of iron and the outer layer contributes the oxygen. It is therefore believed that this layer is in fact FeO . The difference in appearance from the inner layer of Sample 1 (also FeO) is due to temperature and the formation of boundaries within the FeO layer.

Figure 3.4 through Figure 3.9 display significantly reduced oxide layers. However, as stated in section 1.3, only at an oxygen partial pressure of 10^{-12} atm should there begin to be any difference in the scale, and it would first occur in the Fe_2O_3 (the outer most) layer. The reduced oxide layers in these samples may be due to the introduction of flowing gas in the reduced oxygen atmospheres, yet oxygen would still be present to form oxides. This study clearly demonstrated that in all six conditions with reduced oxygen the scale was decreased, yet an effect on total decarburization depth was not apparent. This indicates that diffusion of carbon monoxide through the scale is not a rate limiting step for a given temperature. Moreover, the reduced scale depth also did not substantially increase observed decarburization.

Unlike samples 1 – 3, samples 7 – 9 show an increase in the scale depth as temperature is increased. It is also apparent that the outside oxide layer becomes more porous as temperature is increased, allowing greater diffusion of carbon monoxide through this layer. Nevertheless, the oxide layer is not believed to be the rate limiting step in the decarburization process. This also emphasizes the initial belief that the main contribution in decarburization is from time and temperature. If the scale depth were rate limiting and had a larger effect than temperature, a temperature increase in the 7% O_2 atmosphere would decrease decarburization due to the scale depth increase, despite the additional thermal energy available for diffusion and carbon monoxide formation. This of course assumes scale growth is sufficiently temperature dependent.

4.4 Absence of Trends in Measured Total Decarburization Depth

As the total decarburization depth tables indicate, there is little influence from the oxygen concentration. This is in agreement with findings in literature. However, N. Birks, G.H. Meier, and F.S. Pettit (see reference [6]) predicted decarburization depth would not be altered because the scale depth would also not change, which was stated to control the decarburization. This was not discovered in the current investigation, and thus further work should be conducted to explain this trend. Although it may be argued that the gas flow could cause the observed decrease in scale and that it was not due to the reduced oxygen, this would not explain the reason decarburization was negligibly effected by the reduced scale depth. Equation (29) will predict a depth, but there is no omnipresent effect in the current work.

It is known that the measurements of decarburization depths are largely contingent upon the investigators judgment. In addition, scatter may be present even within one condition repeated several times. These two facts must be considered in explaining any inconsistencies in the measured decarburization depths.

4.5 Future Work

This study focused strictly on the effect of oxygen concentration on decarburization, and not the effect/influence of oxide formation. Although this work served as a basis, the extent that the scale depth and/or composition would have on the decarburization depth was unknown, a priori. Certainly a basis for future work could include careful examination and even focus on the oxide layer and its effect on decarburization for a single oxygen concentration. Such work could include establishing a minimum scale depth at which decarburization is observably altered. Chemical analysis of the different oxide layers would also allow validation or rejection of the proposed oxide layer stoichiometries discussed earlier. Although briefly covered in this paper, calculation of rate constants for the material and oxygen concentrations could also be investigated, but in more detail. More accurate rate constants would allow improved carbon concentration profile predictions. In this study, they were simply used after the experiment to see if Equation (11) would accurately predict the profile.

Another candidate of future work could include the investigation of decarburization in 300M alloy below 727 °C to confirm or refute the formation of the ferrite layer preventing significant decarburization during heating. Any decarburization occurring below this temperature was ignored during predictions, and thus knowledge of the extent of this decarburization would be helpful. On the other hand, a study where samples were exposed to only the dwell temperatures would allow similar effects to be established. Either route would allow the effect of heating and cooling on decarburization to be determined. It is also suggested that future microhardness tests utilize a Knoop microhardness test rather than a Vickers. It was observed that in areas displaying large concentration gradients, i.e. surface regions, the diamond indentation was at times not symmetrical. The side closer to the center of the sample appeared slightly elongated due to the local decrease in hardness. Because in a Knoop hardness test only the long diagonal is measured, this problem would be eliminated if indentations were lined up parallel to the surface.

5. Summary and Conclusions

Samples of 300M were decarburized in air, 14% O₂ (balance of N₂), and 7% O₂ (balance of N₂) at temperatures of 800, 900, and 1000 °C. The time at these temperatures, 2 hours, was held constant for all samples. The ferrite layer (complete decarburization) depths were estimated and Vickers microhardness tests conducted prior to austenitizing all samples at 1000 °C for 30 minutes in a vacuum environment and subsequent quenching. The hardened samples were also microhardness tested and an enhanced hardness profile was observed. In addition, the oxide layers were measured. The decarburization depths were compared to values estimated from classical error function-based equations both with and without the contribution of scale. There proved to be reasonable agreement in both cases, with increasing accuracy as the temperature of the heat treatment increased. Finally, an algorithm was created to predict decarburization depth for the study's atmospheric conditions and temperature ranges, which consisted of inputs for atmospheric oxygen concentration, time, and temperature.

From this study, the following was found:

- 1) Temperature had the largest affect on total and complete decarburization of 300M alloy steel, as literature predicted. Although variations existed within a given temperature, the influence of temperature was nonetheless quite apparent despite alteration of the oxygen concentration.
- 2) The oxygen content of the atmosphere had little to no effect on decarburization depth. However, at 800 °C the two reduced oxygen atmospheres did appear to lead to a deeper and more interconnected complete decarburization (ferrite) layer. The absence of a solid ferrite layer in the 800 °C in air sample (Sample 1) suggests complete decarburization may not have occurred, but surface microhardness readings were similar to values obtained from surface values of gross total decarburization surfaces, i.e. all 1000 °C samples.

3) The scale depth decreased dramatically in both the 14% O₂ and 7% O₂ atmospheres, regardless of temperature, in comparison to air. It was found that the scale depth had no affect on decarburization depths, with the exception of the ferrite depth at 800 °C. It was therefore concluded that the diffusion of carbon monoxide through the oxide layer was not a rate limiting step. The air samples displayed nearly equal scale depths despite temperature.

6. Literature Cited

- [1] Carroll, R. I. and J. H. Beynon. "Decarburisation and Rolling Contact Fatigue of a Rail Steel." *Wear*, 260 (2006): 523-537. *Science Direct*. Web. 05/04/2010.
- [2] Sachs, K. "Decarburization: Definition and Measurement." In *Decarburization: the Proceedings of the One-day Conference on Decarburization Organized Jointly by the Heat Treatment Joint Committee of the Iron and Steel Institute, the Institute of Metals, and the Sheffield Metallurgical and Engineering Association, and Held at the Inter-Group Laboratories of the BSC (BISRA), Sheffield, on October 28th, 1969*. London: Iron and Steel Institute, 1970, 13-33. Print.
- [3] Iwase, K., and T. Mochido. "Decarburized Structures of Steels." *The Research Institute for Iron, Steel, and Other Metals* 517 (1948). Web. 05/27/2010. <<http://ir.library.tohoku.ac.jp/re/bitstream/10097/26235/1/KJ00004195456.pdf>>
- [4] Birks, N. "Mechanism of Decarburization." In *Decarburization: the Proceedings of the One-day Conference on Decarburization Organized Jointly by the Heat Treatment Joint Committee of the Iron and Steel Institute, the Institute of Metals, and the Sheffield Metallurgical and Engineering Association, and Held at the Inter-Group Laboratories of the BSC (BISRA), Sheffield, on October 28th, 1969*.. London: Iron and Steel Institute, 1970, 1-12. Print.
- [5] Beaumont, R. "Recent Works Experience." In *Decarburization: the Proceedings of the One-day Conference on Decarburization Organized Jointly by the Heat Treatment Joint Committee of the Iron and Steel Institute, the Institute of Metals, and the Sheffield Metallurgical and Engineering Association, and Held at the Inter-Group Laboratories of the BSC (BISRA), Sheffield, on October 28th, 1969*. London: Iron and Steel Institute, 1970. 34-53. Print.
- [6] Birks, N., G. H. Meier, and F. S. Pettit. *Introduction to the High-temperature Oxidation of Metals*. 2nd ed. New York: Cambridge University Press, 2006. 23, 83-86, 151-157. Print.
- [7] Baud, J., A. Ferrier, J. Manenc and J. Bénard. "The Oxidation and Decarburizing of Fe-C alloys in Air and the Influence of Relative Humidity." *Oxidation of Metals*, 9 (1975): 69-97. *SpringerLink*. Web. 06/032010.
- [8] Stout, R. D. and T. Aho. "Surface Effects Accompanying the Heating of Carbon Tool Steel in Oxidizing Atmospheres." *Controlled Atmospheres*. Proc. of the Twenty-third Annual Convention of the American Society for Metals, Philadelphia. Cleveland: American Society for Metals, 1941. Print.

- [9] Leprince, G., V. Lanreri, P. Henry, R. Cado, and J. P. Riegert. "Experimental Study and Modeling of Oxidation-Decarburization Phenomena in Spring Steels." *Revue de Metallurgie, Cahiers D'Inormation Techniques (France)*, 97 (1997): 200-201. *Corrosion Abstracts*. Web. 06/07/2010.
- [10] Stratton, P. "Strategies for Eliminating Decarburization." *Industrial Heating*, 76 (2009): 48-50. *ProQuest*.. Web. 06/07/2010.
- [11] Callister, W. D. *Fundamentals of Materials Science and Engineering*. 2nd ed. Hoboken, NJ: Wiley, 2005. 164. Print.
- [12] Porter, David A., and K. E. Easterling. *Phase Transformations in Metals and Alloys*. 2nd ed. London: Chapman & Hall, 1992. 75. Print.
- [13] Jones, Denny A. *Principles and Prevention of Corrosion*. 2nd ed. Upper Saddle River, NJ: Prentice Hall, 1996. 411, 424. Print.
- [14] Gaskell, D. R. *Introduction to the Thermodynamics of Materials*. 4th ed. New York: Taylor & Francis, 2003. 359. Print.
- [15] Smith, W. F. *Structure and Properties of Engineering Alloys*. New York: McGraw-Hill, 1993. 159. Print.
- [16] "Methods of Measuring Decarburization, SAE J419." SAE International, Warrendale, PA, 1983. Web. 02/02/2009. <www.ihs.com>
- [17] ASTM Committee EO4.14, "ASTM E1077 – 01(2005) Standard Test Methods for Estimating the Depth of Decarburization of Steel Specimens," ASTM International, West Conshohocken, PA, 2005. Web. 4 June 2010. <www.astm.org>
- [18] Huang, Liping. "Lecture 5: Solution to Diffusion Problems III." MTLE-6060 Advanced Kinetics. Rensselaer Polytechnic Institute, Troy. 02/09/2010. Lecture.

7. Appendices

7.1 Appendix A

Graphical Depiction of a Fourier Series Solution to Fick's Second Law

Solving for Fick's Second law as a Fourier series yields the following equation:^[18]

$$C(x, t) = \frac{4C_0}{\pi} \sum_{j=0}^{\infty} \left[\frac{1}{2j+1} \sin \left(\frac{(2j+1)\pi}{h} x \right) \right] \exp \left\{ - \left(\frac{(2j+1)\pi}{h} \right)^2 Dt \right\}$$

where C is the carbon concentration, j is an integer from 0 to 39 in this case (40 terms), D is the diffusion coefficient at the particular temperature, t is the time, h is the sample width, and x is the distance from the surface. Each successive term is smaller than the one previous to it, and thus after a short period of time only a few terms are actually required to accurately predict a carbon concentration profile. The figure below closely resembles that depicting the error function in Figure 1.1.

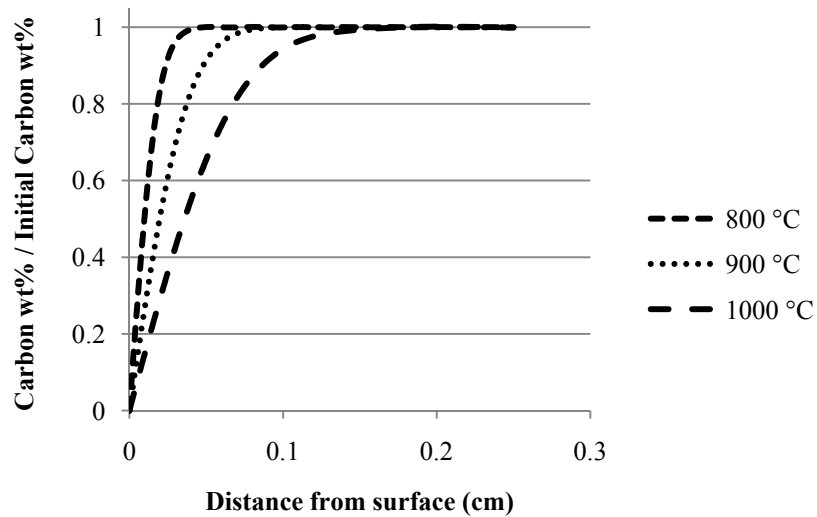


Figure 7.1: Concentration gradient of a carbon steel created from a Fourier series

7.2 Appendix B

Hardness profiles prior to austenitization and quenching

The following plots represent the hardness gradients observed in the samples prior to austenitization and quenching (non-hardened). It should be noted that hardening greatly increases differences between the surface and bulk hardness, as can be seen when comparing the following plots to those found in Figure 3.16 through Figure 3.24. Scatter also becomes more dramatic in the non-hardened profiles. In the non-hardened form, pearlite is very apparent. Therefore, some indents may take place in the very soft ferrite, and others may indent mainly in cementite. To compensate for this, large loads may be used at the cost of resolution.

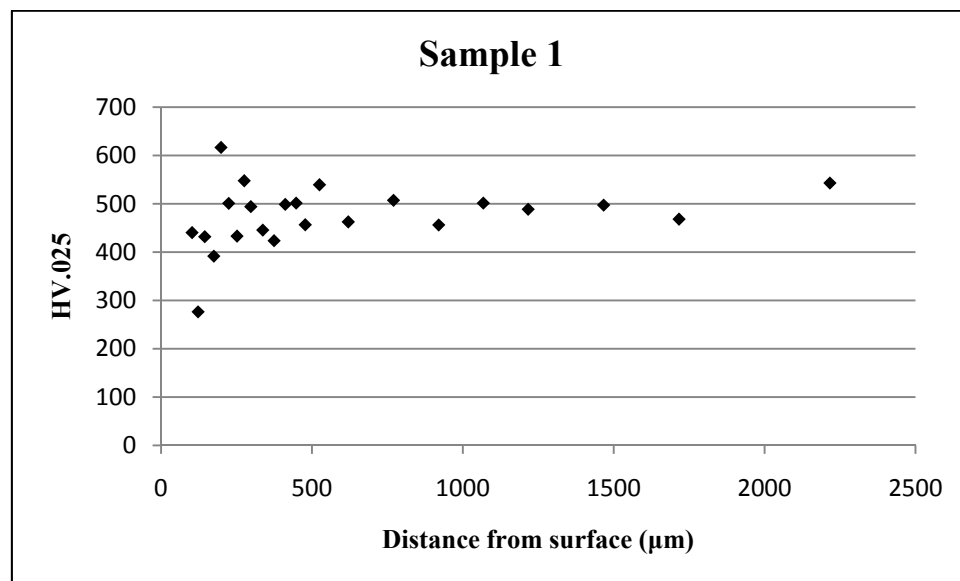


Figure 7.2: Hardness profile prior to austenitization and quenching of Sample 1

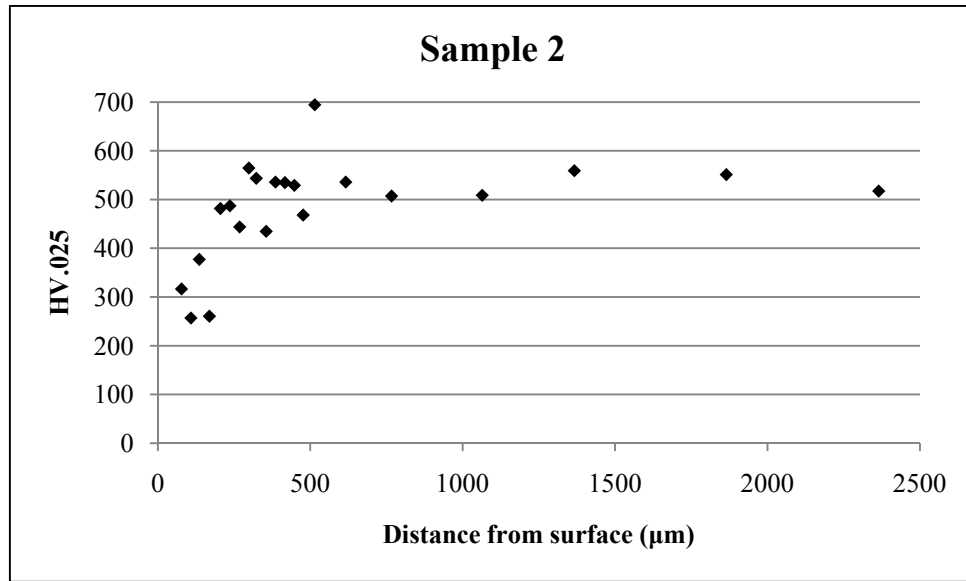


Figure 7.3: Hardness profile prior to austenitization and quenching of Sample 2

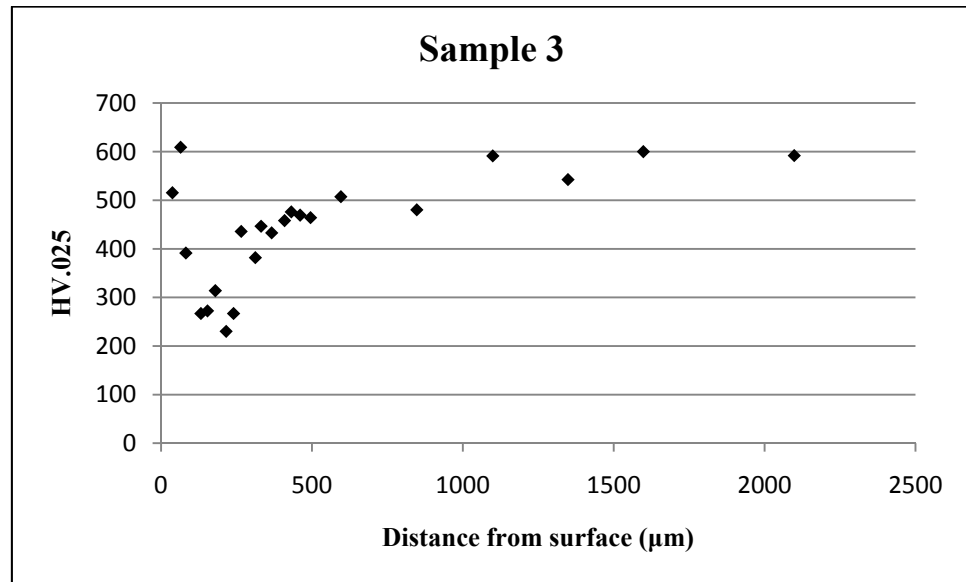


Figure 7.4: Hardness profile prior to austenitization and quenching of Sample 3

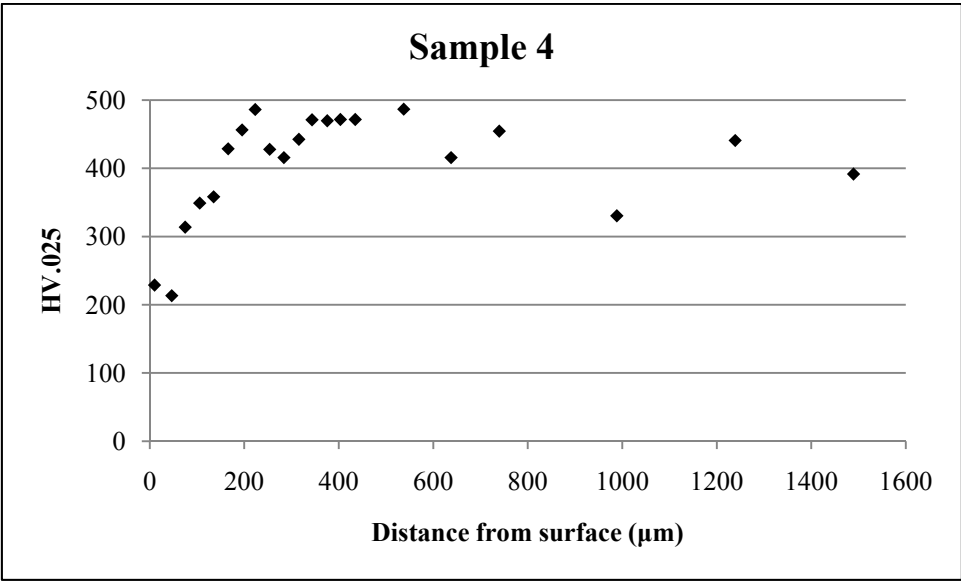


Figure 7.5: Hardness profile prior to austenitization and quenching of Sample 4

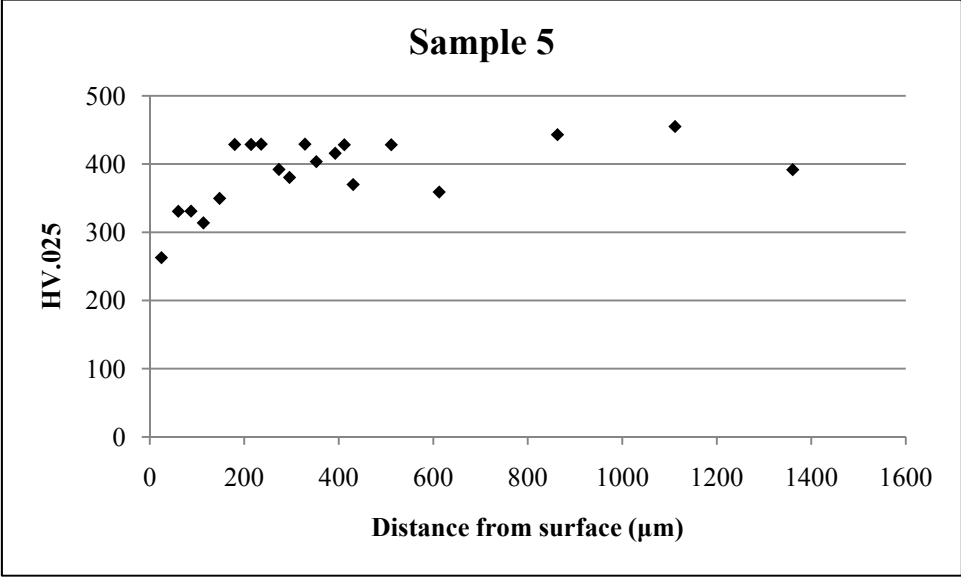


Figure 7.6: Hardness profile prior to austenitization and quenching of Sample 5

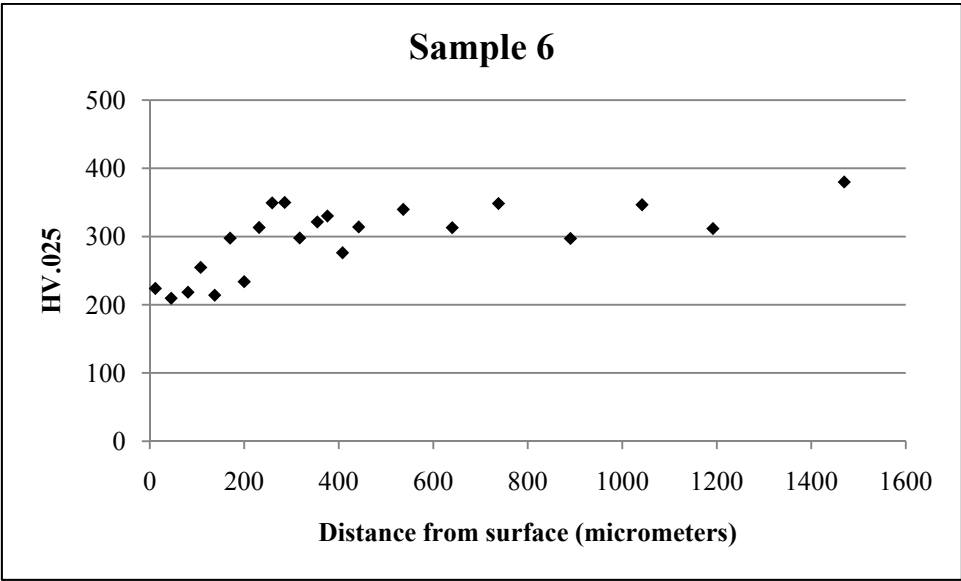


Figure 7.7: Hardness profile prior to austenitization and quenching of Sample 6

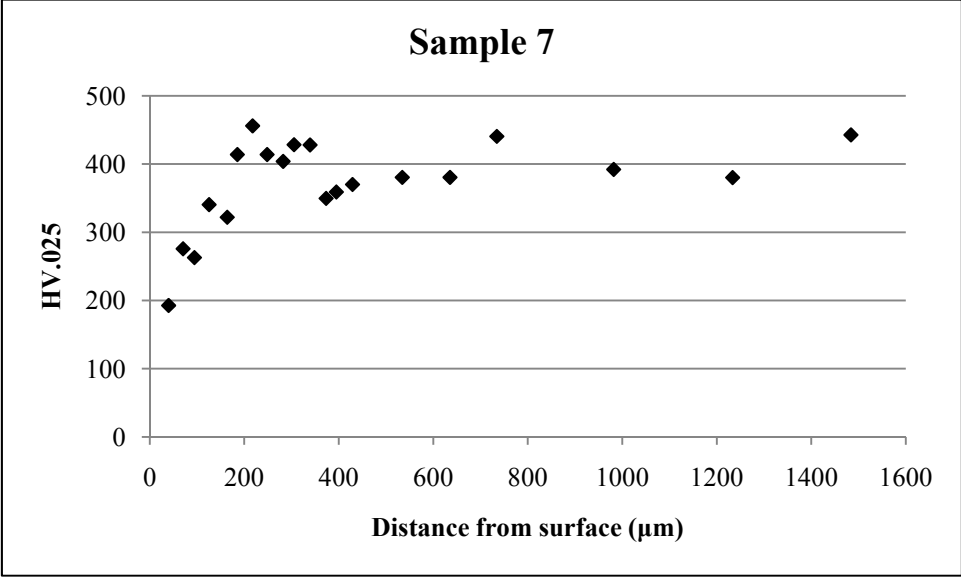


Figure 7.8: Hardness profile prior to austenitization and quenching of Sample 7

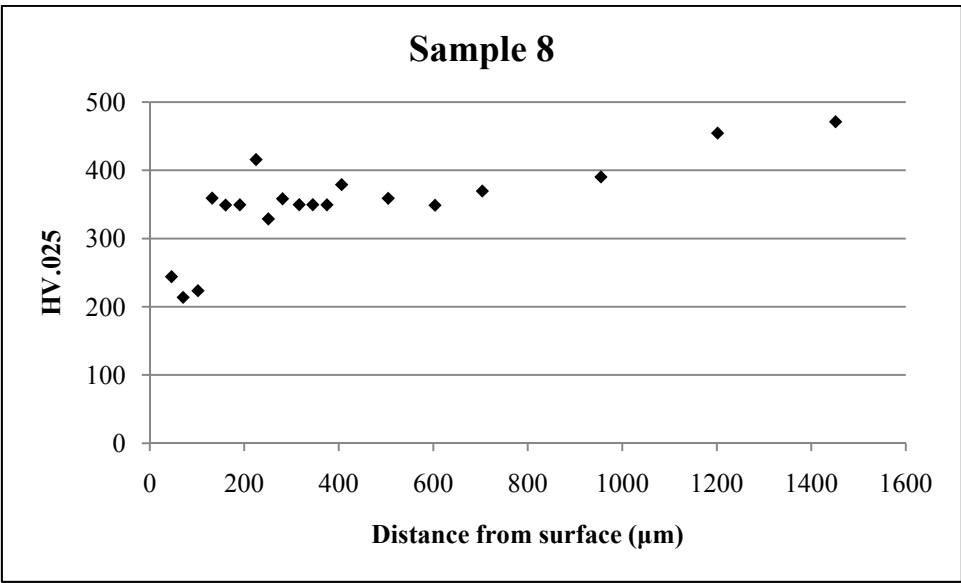


Figure 7.9: Hardness profile prior to austenitization and quenching of Sample 8

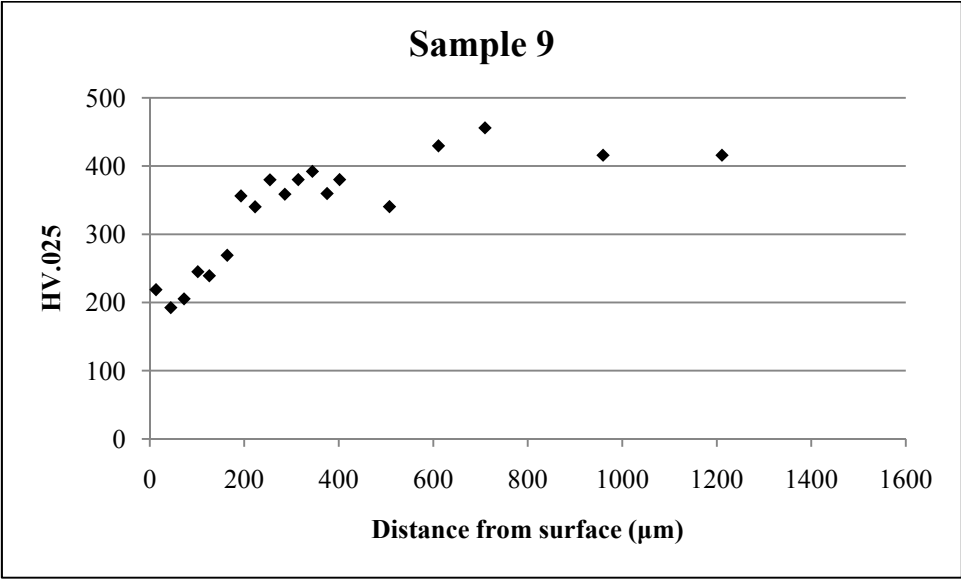


Figure 7.10: Hardness profile prior to austenitization and quenching of Sample 9

7.3 Appendix C

Additional micrographs of pre-hardened samples

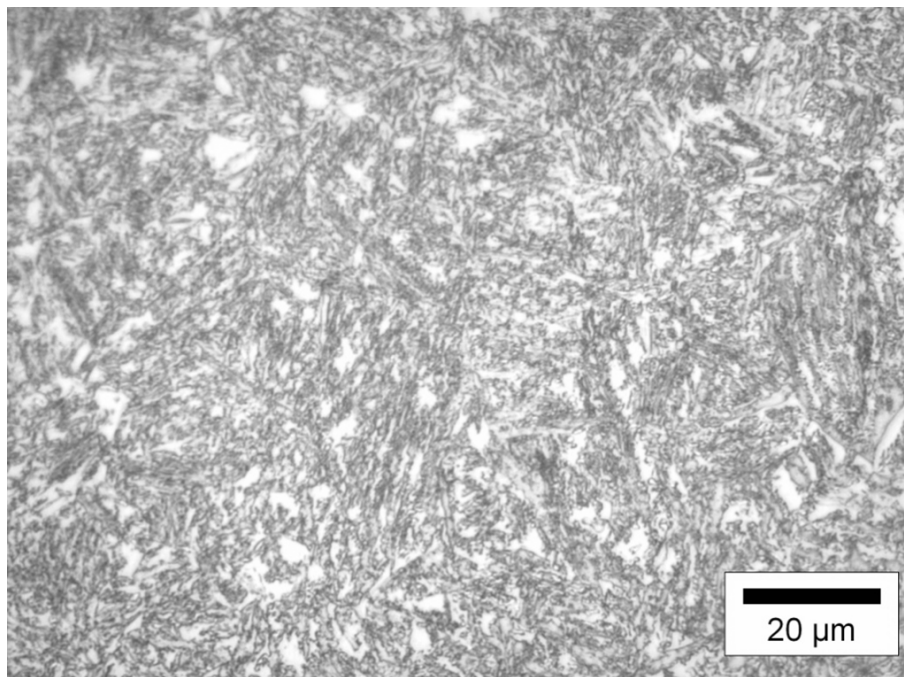


Figure 7.11: Micrograph of Sample 1 (800 °C in air, furnace cooled)

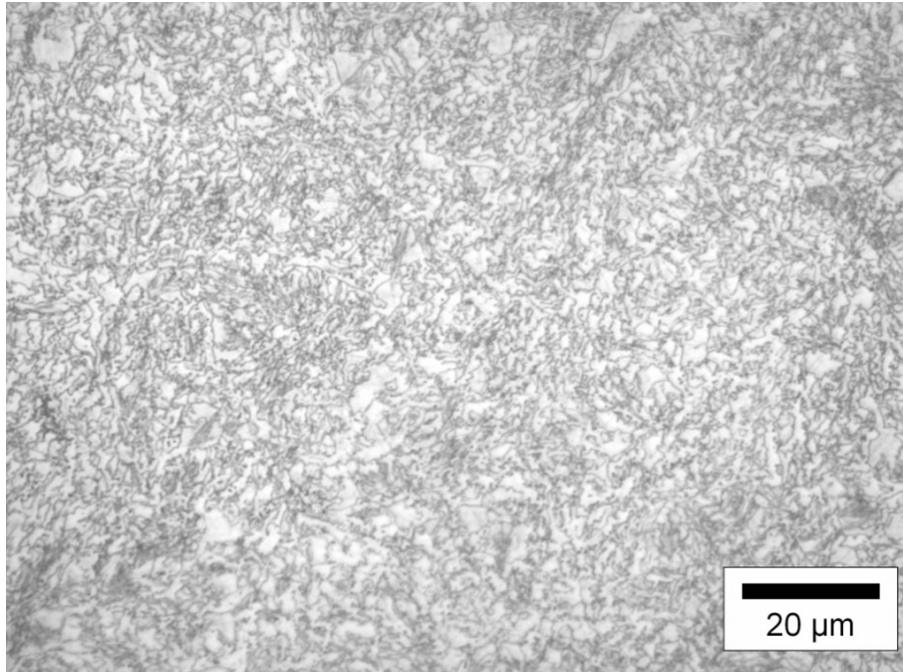


Figure 7.12: Micrograph of Sample 2 (900 °C in air, furnace cooled)

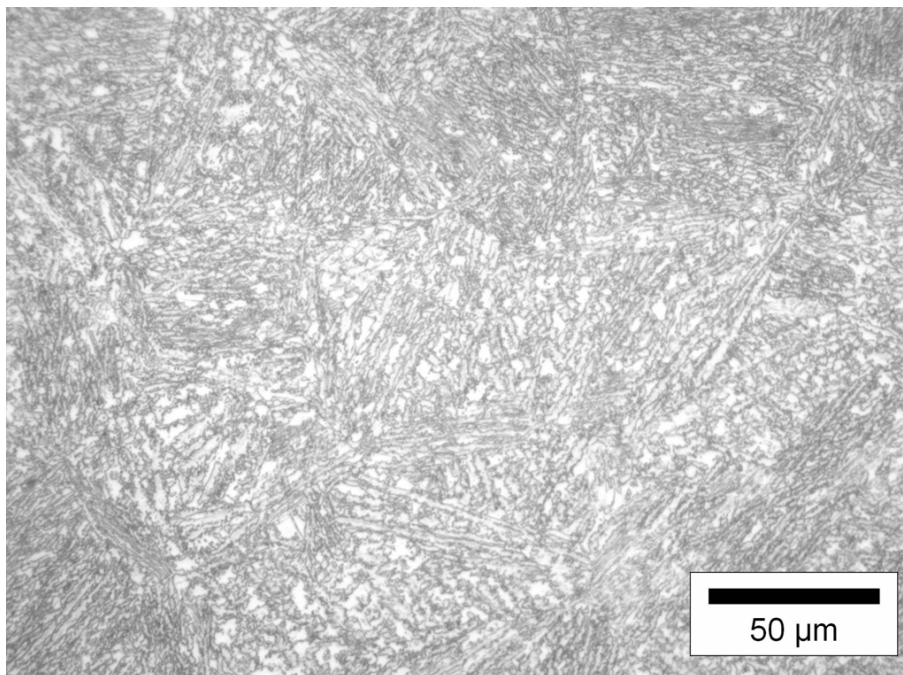


Figure 7.13 Micrograph of Sample 9 (1000 °C in 7% O₂, balance nitrogen, furnace cooled)

7.4 Appendix D

Calculated values of the parabolic rate constant for oxide layers

The following are the calculated values of the parabolic rate constant, k_c , for the growth of the oxide layers using the equation presented previously:

$$k_c = \frac{X^2}{2t}$$

Values were calculated by use of the scale depth and time of $t = 7200$ s. Although the oxide layer would also grow during heating and cooling at elevated temperatures, this was not incorporated. Therefore, the following represents overly simplified values used to allow rough estimation of the carbon profile. It should be observed that there are no apparent trends.

Table 7.1: Parabolic rate constants calculated from scale depths

Sample	Scale (μm)	k_c ($10^{-6}\text{mm}^2/\text{s}$)
1	114	0.908
2	85	0.503
3	112	0.878
4	35	0.084
5	40	0.112
6	88	0.537
7	22	0.034
8	63	0.276
9	64	0.282